Contribution of cytoplasm viscoelastic properties to mitotic spindle positioning

Jing Xie[1,2,*], Javad Najafi[1,2,*], Rémi Le Borgne[1], Jean-Marc Verbavatz[1], Catherine Durieu[1], Jeremy Sallé[1,2]

and Nicolas Minc[1,2,#]

[1]Université de Paris, CNRS, Institut Jacques Monod, F-75006 Paris, France

[2] Equipe Labellisée LIGUE Contre le Cancer

[#] Corresponding author: Nicolas Minc, nicolas.minc@ijm.fr

[*] Equal contribution

Author Contributions: Conceptualization, N.M., J.X. and J.N.; Methodology, N.M., J.X., J.N., R.L., C.D., J.M.V. and J.S. Writing –Original Draft, N.M., and J.X. Draft Editing. N.M., J.X., J.N and J.M.V.

Competing Interest Statement: The authors declare no conflict of interest.

Classification: PHYSICAL SCIENCES; Biophysics and Computational Biology; BIOLOGICAL SCIENCES; Cell Biology

Keywords: Cell division; Mitotic spindles; Forces; Cytoplasm; Flows

ABSTRACT

Cells are filled with macromolecules and polymer networks that set scale-dependent viscous and elastic properties to the cytoplasm. Although the role of these parameters in molecular diffusion, reaction kinetics and cellular biochemistry is being increasingly recognized, their contributions to the motion and positioning of larger organelles, such as mitotic spindles for cell division remain unknown. Here, using magnetic tweezers to displace and rotate mitotic spindles in living embryos, we uncovered that the cytoplasm matrix can impart viscoelastic reactive forces that move spindles, or passive objects with similar size, back to their original position. These forces are independent of cytoskeletal force generators, yet reach hundreds of piconewtons and scale with cytoplasm crowding. Spindle motion causes the cytoplasm to shear and rearrange, dissipating elastic energy and limiting spindle recoils with functional implications for asymmetric and oriented divisions. These findings suggest that bulk cytoplasm material properties may constitute important control elements for the regulation of division positioning and cellular organization.

Significance Statement

The regulation of mitotic spindle positioning is a key process for tissue architecture, embryo development and stem cells. To date, most models have assumed that spindles are positioned by forces exerted by polar cytoskeleton networks, like microtubule asters or acto-myosin bundles. Here, using in *in situ* magnetic tweezers to apply calibrated forces and torques to mitotic spindles in live dividing sea urchin cells, we found that the viscoelastic properties of the cytoplasm medium in which spindles are embedded can hold spindles in place, and move them back if their original position is perturbed. These viscoelastic forces are large and may significantly participate in the force balance that position and orient mitotic spindles in many cell types.

Main Text

Introduction

The cytoplasm is a heterogeneous composite material crowded with large macromolecular complexes, endomembranes, and entangled cytoskeletal networks (1-3). These set a hierarchy of pore and mesh sizes which define rheological properties, such as viscosity and elasticity, that impact fundamental processes ranging from the kinetics of biochemical reactions to vesicular transport and cell shape control (4-6). The importance of cytoplasm material properties for cellular physiology has been recognized and studied for decades, starting from early micro-rheology experiments by Crick or Hiramoto (7-9). These showed that injected micrometric beads displaced in the cytoplasm exhibit typical viscoelastic responses, with partial positional feedback that move them back towards their initial position. Thus, the cytoplasm features both solid-like and fluid-like behavior, with bulk elastic moduli on the order of ~1-10 Pa, typical of soft gels and viscosities 100-1000 times that of water. More recent studies have now established that these rheological characteristics exhibit size, force or frequency dependence, and provided more refined descriptions of the cytoplasm using frameworks of non-linear viscoelasticity or poroelasticity (3, 5, 10-13). Object size is of particular relevance, given that components floating in the cytoplasm may range over 4-5 orders of magnitudes. Indeed, cytoplasm rheology has been proposed to transit from that of a Newtonian fluid for small particles to that of a more glassy or elastic solid for larger elements (12, 14). To date, however, many studies of bulk cytoplasm properties and their functions have focused on relatively small objects, leaving the fundamental problem of how they impact the motion of large organelles, like nuclei or cytoskeletal assemblies poorly explored.

The mitotic spindle is one such large assembly that resides at a precise location in the cytoplasm to specify cytokinesis, and thus the size and position of daughter cells in tissues (15-17). Spindles are built from dynamic microtubules (MTs) and motors and can take up significant portions of cellular space. They are commonly associated with networks of nuclear intermediate filaments and endomembranes that form a so-called spindle matrix (18, 19). These considerations suggest that their motion in the dense cytoplasm matrix could be associated with large viscous and elastic drags, with potential implications for division positioning and chromosome segregation. Until now however, the literature covering the mechanics of spindle positioning has been dominated by the role of active directed forces from polar cytoskeletal networks. Spindles may for instance decenter or rotate, during asymmetric or oriented divisions, a process typically associated with forces generated by contractile acto-myosin networks (20, 21) or astral microtubules (MTs) and associated motors like dynein (22). For symmetric divisions, mitotic spindles reside stably in the cell center. This is thought to be regulated by MTs that grow to contact cell boundaries and exert length-dependent pushing and/or pulling forces on the spindle: when spindles become off-centered, asymmetries in MT lengths and forces act as an effective spring related to cell shape to re-center spindles (23-27). Net forces applied by MT asters or acto-myosin networks may range from few tens to hundreds of piconewtons (pN) (28-30). A displacement of an impermeable objects with the radius of a spindle of R= 5 μm by a distance

d=5 µm, typical of many asymmetric divisions, in a matrix with an elastic modulus of G=1 Pa, like the cytoplasm, would generate a reactive force F=6πR*G*d ~500 pN. Thus, viscoelastic properties of the cytoplasm could in principle be highly relevant to the mechanics of spindle positioning. To date, however, the lack of proper assays to probe cytoplasm rheology at the scale of a moving spindle has impaired testing this fundamental problem for cell organization.

Here, by exploiting large sea urchin cells, where mitotic asters are too short to reach the cell surface, we establish and quantify the direct contribution of bulk cytoplasm viscoelasticity to the mechanics of spindle positioning. We use spindles or large passive oil droplets moved and rotated by calibrated magnetic tweezers in intact cells to probe cytoplasm viscosity and elasticity, at time and length scales representative of spindle movements commonly observed in asymmetric or oriented divisions. We find that the stress exerted by the spindle on the cytoplasm matrix causes it to flow and deform, and exert large reactive spring-like forces that move back this large organelle towards its initial position. Cellular-scale flows also shear and rearrange the cytoplasm matrix, dissipating elastic energy and rendering spindle repositioning time-dependent which facilitates rotational over translational spindle motions. Our results place cytoplasm rheology as a hitherto unappreciated element in the force balance that controls the positioning of mitotic spindle and potentially other large organelles.

Results

Viscoelastic forces maintain metaphase spindle position even in the absence of astral MTs contacting the cortex

In many small cells, mitotic spindles are connected to the cell cortex by dynamic MTs which act as dominant force generators to maintain or modulate spindle position (31). In larger cells, limits in spindle size may prevent bounded metaphase mitotic asters from reaching the cell surface (32-35). Using immunofluorescence and Airy-scan confocal microscopy to detect individual astral MTs around metaphase spindles of 95 µm-sized sea urchin zygotes, we computed a mean distance from astral MTs +tips to the actin-rich cortex of 14.5 +/- 0.2 µm (+/- SEM), which corresponds to ~15 % of egg size. Out of ~4000 MTs tracked we found a mean of only 3.35 +/- 0.74 MTs/cell that came within 5 µm of the egg surface, a distance typically larger than the actin cortex in these eggs (Fig 1A-1B) (36). These results were confirmed by visualizing MTs in live cells with different probes, as well as with transmission electron microscopy of eggs fixed with optimized methods to reveal MTs (Fig S1A-S1D) (37). In sharp contrast, and as previously reported, interphase and anaphase/telophase asters spanned the whole cell with a mean of 373 +/- 7 and 408 +/- 24 MTs/cell reaching a distance less than 5 µm to the surface, respectively (Fig 1C and Fig S1E) (32, 35). In spite of lacking MT contact with the cell surface, the spindle appeared largely static at the cell center in both position and orientation, over the typical ~10 min duration of metaphase, or over longer time-scales when metaphase was prolonged with the proteasome inhibitor MG132 (Movie S1). Thus, metaphase

4

spindles can robustly maintain their position and orientation for long periods of times, even in the absence of astral MTs contacting the cell cortex.

To directly modulate spindle position and orientation, we implemented *in vivo* magnetic tweezers to apply forces and torques to spindles in live cells (28). We injected a specific type of magnetic beads in unfertilized eggs, and added sperm to trigger fertilization (30, 38). These beads exhibit spontaneous centripetal motion along MT asters and form compact aggregates that stay attached to centrosomes through the cell cycle in these cells, allowing to apply calibrated magnetic forces on centrosomes by approaching a magnet tip. The presence of beads at spindle poles did not affect spindle dimensions, and had no notable effect on cell cycle progression (Fig S1F-S1G). In some embryos, beads often split into two aggregates, following centrosome duplication in interphase or early prophase. In others, the beads only tracked one centrosome, allowing a point force application at a single spindle pole (Fig S1H-S1I). Using those, we applied external forces ranging from ~70 to 700 pN along different axis, and monitored resultant spindle motion. Pulling the spindle with an external force parallel to its long axis, caused the spindle to translate towards the magnet tip, while a force applied orthogonal to the spindle axis caused both translational and rotational motions that tended to align the spindle along the magnetic force axis (Fig 1D-1E and 1H-1I, Movie S2 and S3). Therefore, these experiments allowed to recapitulate spindle movements typically observed in asymmetric or oriented divisions with calibrated forces and torques in intact cells.

Astral MTs that grow to the cortex, to push or pull on spindles, may act effectively as an active elastic system related to cell shape that brings back a spindle to the cell center if its position is perturbed (23, 25). In our system, where spindles lack MTs reaching the cell boundaries we anticipated a viscous response to applied forces with no elastic positional feedback. Strikingly, however, the displacement-time curve of spindles moved parallel or orthogonal to their long axis by external forces, exhibited a typical viscoelastic response: spindle motion was first linear at short time-scales below 10-30s, following a viscous regime, but then slowed down, yielding an inflection in the displacement-time curve indicative of internal elastic forces that push or pull back the spindle to oppose external forces (Fig 1F and 1J). Accordingly, larger forces yielded larger displacement at a fixed time point, and when the force was released, the spindle recoiled back (Fig 1G, 1K and Fig S1J). We also noted that at longer time scales above ~100-200 s the curve tended to converge onto another linear regime. In addition, recoils were only partial, with spindles recovering ~ 40-60 % of their initial displacements, often yielding a small asymmetry in division plane positioning (Fig 1G and 1K). These behaviors reflect significant dissipations in the stored elastic energy.

Rotational dynamics of spindles submitted to magnetic torques also exhibited a viscoelastic response, but elastic recoils appeared less pronounced than in translation, causing spindles to tilt and mostly maintain their final orientation at the time of force release (Fig 1L and 1M). Importantly, similar responses were obtained in cells arrested in metaphase with MG132, ruling out putative contributions of aster regrowth and initial cortex contact in late metaphase. Spindle pulling assays were also limited to a small enough

displacement that ensured that mitotic asters did not contact the cortex, and spindle re-centering did not exhibit any correlation with the final distance to the cortex (Fig 1F-1G, 1J-1M and Fig S1K). Thus, although these data cannot firmly reject a minor role of MTs contacting the cortex, they suggest that most of this viscoelastic response may be attributed to elements in the cytoplasm. Together these results suggest the existence of viscoelastic restoring forces that maintain spindle positon and orientation, even in the absence of MTs reaching the cell cortex.

Spindle repositioning is caused by viscoelastic restoring forces from bulk cytoplasm material.

To understand the origin of these viscoelastic restoring forces, we tested the role of MTs and dynein as prominent force-generating systems for mitotic spindle positioning. We displaced spindles with magnetic tweezers, and rapidly rinsed cells with Nocodazole or Ciliobrevin D, to affect MTs or dynein motor activity respectively, and monitored the ability of spindles to recoil back (Fig 2A). In controls, the positional recovery followed a single exponential with a decay time-scale of 103 +/- 41s and an offset of 43 +/- 11%. Nocodazole treated spindles shrank in size to eventually disassemble, over a period of ~5-10 min, but recovered their positions with similar dynamics and offsets as controls. Ciliobrevin D treatment yielded similar response as Nocodazole but with less drastic effect on spindle shape (Fig 2B-2D and Fig S2A-S2F). Therefore, in agreement with the lack of MTs reaching cell boundaries, astral MT polymerization pushing or pulling forces mediated by dynein at the cortex or in the cytoplasm appear to be dispensable for repositioning spindles to the cell center.

To more directly establish that viscoelastic repositioning forces are independent of spindle associated cytoskeletal elements, we sought to recapitulate early micro-rheology assays performed by Crick or Hiramoto (7-9), but using objects that have similar sizes as mitotic spindles. Inspired by experiments performed in mouse oocytes and in Xenopus extracts (29, 39), we embedded hydrophobic magnetic beads in soybean oil, and injected large 30-35 µm oil droplets to move them in the cytoplasm with magnetic tweezers. We purposely used unfertilized eggs, to circumvent the presence of large asters or spindles that could affect droplet motion in the cytoplasm from steric hindrance or by generating active flows and stresses (40) (Fig 2E-2F). In the absence of external forces, oil droplets were immobile in the cytoplasm for long durations of up to 1h, much like female nuclei in these unfertilized eggs (Fig S2G-S2L). Remarkably, droplets exhibited a viscoelastic response to external forces similar to spindles, with a rapid initial constant velocity followed by a saturating elastic regime. Upon force cessation, droplets moved back towards their initial position with similar positional offsets as spindles, but shorter time-scales. Droplets viscoelastic recoil occurred independently of whether the droplet had a more centered or off-centered position suggesting that restoring forces are independent of the initial location of the object in the cytoplasm (Fig 2G-2K and Movie S4). These data suggest that elements in bulk cytoplasm may generate viscoelastic reactive forces that move spindles or similar-sized passive objects back to their initial positions.

6

While mitotic spindles are often pictured as polar networks made of MT filaments, the accumulation of membranous organelles or other nuclear intermediate filaments on their MT network has suggested the existence of a spindle matrix, which could render them more physically akin to an impermeable droplet (18, 41). Accordingly, by performing Serial Block Face electron microscopy, we found that spindles were covered by packed endomembranes, with an "onion peel arrangement" typical of mitotic endoplasmic reticulum (ER) networks (42) (Fig 2L and Movie S5). This endomembrane accumulation is readily evident in DIC images as a smooth area around spindles (Movie S1-S3). Immunofluorescence further validated this accumulation, and segmentation of ER membranes provided an estimate of an upper-bound pore size of 0.2-0.5µm between membranes (Fig 2L-2M). Thus, metaphase spindles may be impermeable to relatively large objects and networks, a property which like oil droplets, allows them to be dragged by viscoelastic flows and forces from bulk cytoplasm.

The cytoplasm applies large elastic and viscous drags to the mitotic spindle.

To quantify restoring stiffness and viscous drags, we fitted experimental data with a three-element Jeffreys' model, which provided the simplest 1D linear model for the observed rising and relaxation curves (43). This model has been employed to describe, among others, the rheology of suspensions of elastic spheres, polymeric liquids, and was previously used to understand viscoelastic properties of the cytoplasm (8, 44, 45). This model features an elastic spring of stiffness κ, in parallel with a dashpot of viscosity γ_1, in series with a second dashpot of viscosity γ_2, defining two characteristic time-scales. The first one, $\tau_1 = \kappa/\gamma_1$ is the time-scale needed for spindle associated flows to charge the elastic elements in the material. The second, $\tau_2 = \kappa/\gamma_2$ sets the rate of plastic yield of these elements or fluidization of the material, which limit elastic restoration and generates an offset in the relaxation (43) (Fig 3A-3B).

Using this model, we computed a restoring stiffness for spindles pulled along their long axis of κ = 55 +/- 6 pN/µm (n=19 cells) and 54 +/- 6 pN/µm for orthogonal pulls (n= 21 cells). This shows that a displacement away from the cell center of 5% of the cell diameter (~4 µm), generates a restoring force of ~250 pN. These are forces equivalent to that generated by hundreds of molecular motors (46). The stiffness measured for oil droplets was twice higher than for spindles, accounting for their shorter relaxation time-scales (Fig 3C and Fig 2J). One possible interpretation is that oil droplets are actuated in an unfertilized cytoplasm previously reported to be twice stiffer than the mitotic cytoplasm (8, 9). An alternative, is that the spindle may be porous to smaller elastic elements in the cytoplasm. These numbers amount to a lower-bound value of the effective bulk modulus, $G = \kappa/6\pi R$, with R the size of spindles, to be on the order of 0.2-0.3 Pa. This is smaller, but in the same range as previous rheological measurements of cytoplasm stiffness in different cell types and extracts (9, 11, 47).

Spindle viscous drags were unexpectedly high with a parallel drag of 4493 +/- 847 pN.s/µm and an orthogonal drag of 4498 +/- 771 pN.s/µm (Fig 3D). Considering reported values of cytoplasm viscosity in

7

these cells (8), they amount to the drag of an object typically ten times larger than the spindle. This enhanced drag could be explained by the confinement of the spindle by cell boundaries which couples hydrodynamically the spindle with the surface and reduces spindle mobility (48, 49). Accordingly, theoretical predictions for a solid object moving in a viscous fluid contained in a sphere, with a radius twice that of the object, yield to a 10-20 fold increase of the object's drag coefficients (50). This suggests that spindle large drags could primarily result from its interaction with the cytoplasm fluid confined by cell boundaries. Overall, these analyses support that the response of spindles to external forces are primarily associated to the viscoelastic properties of the cytoplasm matrix (Fig S3A-S3D).

To compare the efficiency of bulk cytoplasm viscoelastic properties to that of active MT asters and motors, we next measured centering stiffness in anaphase, which follows metaphase by only few minutes. In anaphase, asters regrow to fill the whole cell volume, with an estimate of several hundreds of MTs contacting the cortex (Fig 1C and Fig S1E). Anaphase is thought to imply the largest MT based forces along the cell cycle, as MTs engage with dynein motors at the surface or in the cytoplasm, to separate chromosomes and move asters apart (28, 40, 51, 52). Here, magnetic forces were only applied orthogonal to the spindle axis, as parallel pulls interfered with chromosome force-separation systems (Fig S3E-S3G). While the drags of anaphase spindles were similar to that found for metaphase spindles, a net difference was obtained in term of elastic behavior, with a restoring stiffness for anaphase spindles of 150 +/- 14 pN/µm, nearly three times higher than during metaphase (Fig 3E-3G). These results suggest that bulk cytoplasm restoring forces can amount to an equivalent of ~30% of the maximum MT/dynein based pulling system in these cells.

Cytoplasm forces depend on cytoplasm crowding and bulk F-actin meshworks.

Crowding agents in bulk cytoplasm, that contribute to set elastic and viscous properties may include among others, cytoskeletal networks, endomembranes like Yolk granules and mitochondria, or ribosomes which are highly abundant in the cytoplasm (Fig 2L). As a general assay to affect cytoplasm crowding, we immersed cells ~5 min prior to mitosis in diluted or concentrated artificial sea water (ASW) and pulled spindles at metaphase onset. We limited the amplitude of these shocks to a range in which mitotic spindles length, anaphase and cytokinesis were unaffected, but we noted delays in metaphase in hypertonic treatments (Fig S4A-S4D). A hypotonic treatment in 80% ASW caused water to flow into the cells with a minor cell size increase, and reduced spindle restoring stiffness and drags in this diluted cytoplasm to 50.2% and 49.6% of control values respectively. Conversely, a hypertonic treatment in 110% ASW, shrank cells by ~6% and concentrated the cytoplasm, increasing spindle restoring stiffness and drags to 151.4% and 114.4% of control values, respectively (Fig 4A-4D and Fig S4E-S4H). These results demonstrate that viscoelastic reactive forces applied on spindles are directly related to cytoplasm crowding.

Furthermore, as one element which has been shown to contribute to bulk cytoplasm material properties we tested the role of F-actin (11, 47). Imaging injected labelled utrophin, that binds F-actin, we detected a

significant amount of disordered bulk F-actin meshes that surrounded the spindle, though unsurprisingly, the cortex was the most abundant part of the cell. Similar results were obtained with phalloidin staining (Fig S4I). To affect F-actin, we treated cells with Latrunculin B, which disassembled F-actin within minutes, causing the cell surface to soften and shrivel (Fig 4E and Fig S4J-S4K). In Latrunculin B treated cells, spindle repositioning stiffness was 34 +/- 5 pN/µm, 1.6 times lower than controls and viscous drags were also significantly lower, and in proportion more reduced than elastic values (2 times lower than controls). As a consequence, the time-scales for both rising and relaxing phases in Latrunculin B were shorter than in controls, so that the re-centering dynamics, converged onto a similar positional offset, but occurred faster (Fig 4F-4H and Fig S4L-S4O). Importantly, this effect did not implicate putative acto-myosin contractile forces, as treatment with Blebbistatin to inhibit Myosin II did neither alter restoring stiffness and drags nor spindle repositioning dynamics (Fig 4F-4H and Fig S4I, S4L-S4O). These data suggest that bulk F-actin meshworks may act as important crowders that contribute to ~40-50% of cytoplasm elastic and viscous drags on pulled spindle.

Functional implications of cytoplasm mechanics for asymmetric and oriented divisions.

We next investigated an important feature of spindle response, which is the linear rising phase at long time-scale and the offset in the relaxation, which reflect progressive plastic rearrangements or fluidization of elastic elements in the cytoplasm. A prediction of this effect is that a longer force application should dissipate more elastic energy, allowing spindles to stay further from their initial position when the force is released. Accordingly, in the Jeffrey's model, the relaxation offset, a, depends mostly on the ratio of τ_2 to the duration of force application, T, with $a = \frac{1}{1+\frac{\tau_2}{T}(1-e^{-T/\tau_1})} \sim \frac{1}{1+\frac{\tau_2}{T}}$ for sufficiently large T (Fig 5A). To test this, we arrested cells in metaphase with MG132, pulled spindles and held them for increasing periods of time (Fig 5B). Practically, this implied decreasing the pulling force gradually by progressively distancing the magnet, to avoid spindles moving onto the cortex. Remarkably, spindles held longer progressively lost their recoiling behavior with a well-matched alignment of experimental data on the predicted theoretical curve (Fig 5C-5D and Fig S5A-S5D). Therefore, elastic restoration by the cytoplasm may be very effective at short-time scales to stabilize spindles against random thermal or active forces, but vanishes over longer time-scales to facilitate spindle decentration during asymmetric divisions.

As another important read out of this effect, we found that τ_2 was significantly smaller in rotation than in translation (Fig 5E-5F and Fig S5E-S5H). This was reflected both in the more linear shape of the rising curve under force and in the higher values in the angular relaxation offset as compared to translation for the same spindles (Fig 1L and Fig 5G-5H). Thus, rotating spindles appear to dissipate faster rotationally stored elastic energy, causing spindle reorientation to be less-well restored by the cytoplasm than translation. This effect will tend to favor spindle rotation over translation, allowing for instance active force generators to easily tilt spindles, without translating it. We conclude that the dissipation of spindle elastic restoration by

9

plastic rearrangements in the cytoplasm and their time-dependence may be highly relevant to understand spindle positioning phenotypes.

Large-scale flows of cytoplasm material associated with spindle motions

To understand how the cytoplasm matrix reorganizes in response to spindle motion and forces, we mapped cytoplasmic flows. We tracked cytoplasmic granules of ~1 μm in size with Particle Image Velocimetry (PIV) (movie S6). These elements are larger than measured spindle pore size and are dominated by advection with estimated Peclet numbers exceeding 10^2-10^3, therefore best representing potential rearrangement of entangled elastic meshworks in the cytoplasm. When spindles were pulled along their long axis, the cytoplasm flowed along with the spindle and recirculated, forming large symmetric vortices mirrored along the spindle axis. As spindles relaxed, similar vortices formed but with an opposite rotational direction (Fig 6A-6B and Fig S6A). By computing the local divergence of the flow pattern, which provides a qualitative indicator of how the matrix may contract or expand, we found that the portion of the cytoplasm at the front of a pulled spindle appeared compressed, while the portion at the back was more stretched (Fig S6D-S6E). Vorticities in the flow field allowed to visualize shear, and to extract a time-scale from the inverse of the shear rate, on the order of 570 +/- 85 s, close to the time scales for plastic dissipation τ_2 of spindle viscoelastic response (Fig S6B, S6G and S6K). These data indicate that spindle displacement causes the viscoelastic cytoplasm matrix to locally compress and/or expand and apply reactive elastic forces, and shear away from the spindle front.

In orthogonal pulls, the flow patterns were markedly different, with one dominant large vortex centered around a point located bottom-right in the cell with respect to the pulled spindle pole (Fig 6C and Fig S6F). This vortex was significantly larger than in translation (Fig 6E and Fig S6C, S6H). Furthermore, the divergence map appeared asymmetric orthogonal to the spindle axis, but did not reveal notable left-right asymmetric patterns, plausibly reflecting the reduced ability of the cytoplasm to rotate back spindles (Fig S6I-S6J). In relaxation, the flows were mostly vertical, in agreement with the dominance of a translational over rotational spindle recoil (Fig 6D).Therefore, a spindle rotating in the confined boundaries of a cell, appears to shear rather than compress the cytoplasm matrix (Fig 6F). In light of the differential viscoelastic response of translating vs rotating spindles, these flow analyses suggest that shear fluid stress could cause cytoplasm elements to plastically yield faster than in compression, a process typical of many viscoelastic materials (43). We conclude that the organization of viscoelastic flows in response to spindles moving in a cytoplasm confined by cell boundaries, may have a key impact on mitotic spindle positioning phenotypes (Fig 6F).

Discussion

Function of bulk cytoplasm rheology in the mechanics of spindle positioning.

How spindles are positioned and oriented in embryos and tissues is a fundamental problem for cell and developmental biology highly relevant to the emergence of developmental disorders and cancer (17, 53). One current dogma in many animal cells, is that spindles are placed with respect to cell boundaries by active forces from astral MTs that grow to the cell cortex. Here, by exploring a regime where mitotic MT asters do not reach out to the cortex, we demonstrate that the cytoplasm matrix acts as a viscoelastic medium that hold spindles or other large objects in place, and moves them back if their position is perturbed. Restoring forces are large and shall participate in the force balance positioning spindles and asters, by for instance opposing asymmetric cytoskeleton forces during nuclear or spindle decentration and asymmetric division, or those needed to center asters at fertilization (22, 38, 49). Our findings also suggest that restoring forces vanish faster in rotation than in translation, which we attribute in part to the geometry of rotational shear flows, and anisotropies in plastic yields in the cytoplasm material. Therefore a tilt acquired during force exertion is better maintained than a positional offset. This could allow an asymmetric cortical domain enriched in motors to reorient spindles without creating an asymmetric division, a phenotype commonly observed in many tissues (17, 54, 55).

It is important, however, to outline that at rest, the cytoplasm does not apply any net force, and cannot *a priori* center or decenter spindles, asters or nuclei. In large cells, this is achieved earlier in the cell cycle by interphase MT asters that reach to the cell boundaries, and pre-position centrosomes before metaphase (56). We propose that the cytoplasm matrix holds these prepositioned centrosomes in place (57). As spindles scale with cell size, cytoplasm rheology could very well be also relevant to spindle positioning in smaller cells lacking proper mitotic asters, or in which astral MTs do not reach the cell surface (58-60). However, an important open question, is how much these properties contribute in cells where numerous MTs clearly contact the cortex to exert forces that stabilize asters or spindles (28, 38). One possibility is that the impact of cytoplasm elasticity is reduced as astral MTs and motors push back organelles and network away from spindles, effectively confining elastic elements to a zone much closer to the cortex. Another possibility, which we favor, is that transport by motors along MTs could fluidize the cytoplasm space occupied by mitotic asters, effectively decreasing the elastic response of the cytoplasm (61). Further work will be required to understand how active polar cytoskeleton forces and material properties of bulk cytoplasm are integrated to regulate cell division and organization.

Probing cytoplasm material properties at the scale of mitotic spindles.

The cytoplasm is a complex material, whose rheological properties and their impact on cellular functions are emerging as important concepts in cell biology. Here, we probed cytoplasm rheology at scales and speeds, typical of physiological mitotic spindle repositioning and reorientation. In line with previous rheological description of the cytoplasm for small objects (8, 9), we find that a simple linear 1D viscoelastic Jeffreys' model can predict key rheological behavior including rising and relaxation curves, and time-

11

dependent elastic dissipation. Although this suggests that we can treat the effect of the cytoplasm as that of an "inert" Jeffreys' material, these physical properties, are likely dictated and regulated by energy-driven active metabolic processes and random motor motion (4, 11, 13, 14). We also envision that more advanced non-linear viscoelastic or poroelastic description of the cytoplasm could capture many of the features we report in here. Elasticity could for instance be graded, being stiffer close to the cortex and softer in the cell interior, due to the progressive stacking of organelles and networks. Inspections of electron micrographs do not immediately support this view, at least in this system. In addition, viscoelastic recoils of droplets moved from different initial locations in the cell (not only the cell center) suggest a more homogenous elasticity (Fig 2K). Poroelasticity would picture the cytoplasm matrix as a porous elastic solid, with a small pore size bathed in cytosolic liquid (5, 62). As spindles would compress this poroelastic matrix, slowly dissipating pressure gradients would form and push back spindles in place.

Beyond physical frameworks to describe cytoplasm rheology, another important question is which elements define relevant material properties of the cytoplasm at the spindle scale. Meshworks of bulk F-actin filaments contributed to a fraction of ~40-50% of viscous and elastic behavior, acting as one important crowding agent at this scale. Intermediate filaments, like keratin or vimentin could not be tested here, but have been proposed to influence elastic properties of egg cytoplasm extracts (47). In addition, we propose that organelles like mitochondria, yolk granules or lysosomes could behave as dense suspensions of small elastic colloids, which generate mesoscopic elasticity as is known for classical suspension such as paints or bitumen (44). Further experiments of cytoplasm reconstitution will be required to determine which of these elements are dominant or dispensable at the spindle scale, or assay the role of their potential interactions.

Finally, our experiments comparing spindles and oil droplets, raise interesting questions on the physical nature of the mitotic spindle itself. In the context of our assays, we propose that spindles behave as objects impermeable to components larger than a fraction of a micron. Recent report suggest that small particles of ~10nm in size can diffuse in and out of spindles (61). Spindles may thus be largely porous to proteins and molecular complexes such as ribosomes, so that elastic and viscous forces they experience may only arise from the response of larger organelles and networks in the cytoplasm. Mitotic spindles also feature important elastic properties, with axial stiffness measured *in vitro* to range around 80-900 pN/µm (63). In our experiments, we detected minor lengthening of mitotic spindles under force, which amounted to similar values (data not shown). Recent experiments on MT asters also support models of more porous or elastic structures with important implications for mechanisms of centrosome movement (40). By bringing numbers which have been largely missing in the literature, force measurements within live cells will strongly impact our understanding of the very basic mechanisms of cell organization and morphogenesis.

Acknowledgment

Material and Methods

Sea urchin gametes

Purple sea urchins (*Paracentrotus lividus*) were obtained from Roscoff Marine station (France) and maintained at 16°C in aquariums of artificial sea water (ASW; Reef Crystals, Instant Ocean). Gametes were collected by intracoelomic injection of 0.5 M KCl. Sperm was collected dry and kept at 4°C and used within 1 week. Eggs were rinsed twice with ASW, kept at 16 °C, and used on the day of collection. Unfertilized eggs were transferred and adhered on protamine-coated glass-bottom dishes (MatTek Corporation) after removing the jelly coat through an 80-µm Nitex mesh (Genesee Scientific), injected and fertilized under the microscope.

Chemical inhibitors

Inhibitors were prepared in 100X stock aliquots in dimethyl sulfoxide (DMSO). To block metaphase, eggs were incubated for 30 min in 50 µM MG132 (Sigma-Aldrich) before fertilization. Nocodazole (Sigma-Aldrich) and Ciliobrevin D (EMD Millipore), were respectively applied ~3 min and ~5 min before spindle relaxation at a final concentration of 20 µM and 50 µM, respectively. Latrunculin B (Sigma-Aldrich) was added ~5 min before pulling the spindle at a final concentration of 20 µM. Blebbistatin (Sigma-Aldrich) was added 15 min post fertilization at a final concentration of 100 µM.

Hypotonic and Hypertonic shocks

To manipulate cytoplasm density with hypotonic or hypertonic shocks, ASW was prepared to 80% or 110% of its normal content, respectively, by adjusting the amount of DI water to salts mixtures. Eggs were rinsed with these different water at prometaphase, typically 5 min before force application. At these sea water concentrations, cells formed normal spindles and underwent a normal cytokinesis. Metaphase was longer in concentrated ASW. Much lower concentration of 50% ASW were also assayed, but led to large leaks of cytoplasm from the site of injection that dragged spindles out of cells. Higher concentration of 120% or 150% ASW led to cytokinesis failure.

Immunostaining

Immunostaining was performed using procedures described previously (35). Samples were fixed for 70 min in 100 mM Hepes, pH 6.9, 50 mM EGTA, 10 mM MgSO4, 2% formaldehyde, 0.2% glutaraldehyde, 0.2% Triton X-100, and 400 mM glucose. To reduce autofluorescence, eggs were then rinsed 3 times in PBS and placed in 0.1% NaBH4 in PBS freshly prepared, for 30 min. Eggs were rinsed with PBS and PBT (PBS + 0.1% TritonX) and blocked in PBT supplemented with 5% goat serum and 0.1% bovine serum albumin (BSA) for 30 min. Samples were rinsed with PBT before adding primary antibodies. For MT staining, cells were incubated for 48 h at 4°C with a mouse anti-α-tubulin (DM1A; Sigma-Aldrich) primary antibody at 1:5,000 in PBT, rinsed 3 times in PBT and incubated for 4 h at room temperature with anti-mouse secondary antibody coupled to Dylight 488 (Thermo Fisher Scientific) at 1:1,000 in PBT for 4-5h. For ER staining, samples were treated with a rabbit anti-KDEL (Invitrogen) primary antibody at 1:2,000 in PBT, for 48h, rinsed in PBT and incubated with an anti-rabbit secondary antibody coupled to Dylight 650 (Thermo Fisher Scientific) at 1:1,000 in PBT. To stain F-actin, samples were incubated for 1h in a solution of Rhodamine Phalloidin at 4U/ml in PBT. Eggs were washed three times in PBT then twice in PBS, transferred in 50% glycerol in PBS, and finally transferred into mounting medium (90% glycerol and 0.5% N-propyl gallate PBS). Fixations of cells treated with Nocodazole, Ciliobrevin D, and Latrunculin B were performed 10 min after adding the drug (Fig S2F).

Fixation for electron microscopy

To visualize astral MTs around spindles, one cell stage zygotes were fixed in metaphase (1h post-fertilization) in 0.4M sodium acetate, 2% glutaraldehyde (Electron Microscopy Sciences) during 30sec and in 0.4M sodium acetate, 2% OsO4 (Electron Microscopy Sciences) during 30min (Asnes and Schroeder, 1979), and transferred for 1h to 2% glutaraldehyde, 1% Osmium, then washed 15 min with the same buffer and 2 x 15 min in water. Dehydration was performed using graded concentrations of ethanol in water for 10 min each. Resin infiltration was performed by incubating 30 min in a 30% Agar low viscosity resin (Agar Scientific Ltd), then 30 min in a 50% Agar low viscosity resin, 30 min in a 75% resin followed by a 1h and overnight incubation in pure resin. The resin was then changed twice and the samples were incubated for 1 hour prior to inclusion in BEEM capsules and 18 hours polymerization at 60 °C. 70 nm sections were obtained using an EM UC6 ultramicrotome (Leica), and post-stained in 4% aqueous uranyl acetate followed by lead citrate.

For ER endomembrane visualization by Serial Block Face electron microscopy , one cell stage zygote were fixed in metaphase in 0.2M cacodylate buffer, 0.25M sucrose, 2% paraformaldehyde, 2% glutaraldehyde during 1h and progressively transferred in 0.2M cacodylate buffer, 0.35M NaCl, and stored at 4°C until processing. Samples were then prepared for Serial Block Face using the NCMIR protocol (https://ncmir.ucsd.edu/sbem-protocol). They were washed 3 times with cold cacodylate and post-fixed for 1 hour in a reduced osmium solution containing 1% osmium tetroxide, 1.5% potassium ferrocyanide in 0.15 mM sodium cacodylate buffer, followed by incubation with a 1% thiocarbohydrazide (TCH) solution in

water for 20 min at room temperature (RT). Subsequently, samples were fixed with 2% OsO_4 in water for 30 min at room temperature, followed by 1% aqueous uranyl acetate at 4 °C overnight.

The samples were then subjected to *en bloc* Walton's lead aspartate staining (2) at 60 °C for 30 min. Then, samples were dehydrated in graded concentrations of ethanol for 10 min each. The samples were infiltrated with 30% Agar low viscosity resin (Agar Scientific Ltd) for 1 hour, 50% Agar low viscosity resin for 2 hours and 100% Agar low viscosity resin overnight. The resin was then changed and the samples further incubated during 3 hours prior to inclusion in BEEM capsule Bottle Neck tips (EMS) and polymerized for 18h at 60 °C. The polymerized blocks were mounted onto special aluminum pins for SBF-SEM imaging (FEI Microtome 8mm SEM Stub, Agar Scientific), with Two part conduction silver epoxy kit (EMS, 190215).

Live-probe for the cytoskeleton

TauMBD-mCherry constructs were expressed in BL21 (DE3)-RIL (Agilent) cells, purified on a Ni-NTA resin (Invitrogen) and dialyzed with PBS buffer using a 10000MWCO dialysis cassette (ThermoScientific). Tubulin-Atto565 was a gift from Benjamin Lacroix. Tubulin was purified from pig brains and labelled with NHS-ester-ATTO 565 (ATTO-TEC) (Lacroix et al., 2018). UtrCH-AlexaFluor488 was a gift from Peter Lenart. UtrCH recombinant protein was expressed in *E.coli*, purified on a Ni-NTA resin (Qiagen), and labelled with AlexaFluor 488 succinimidyl ester (Invitrogen) (64).

Magnetic force application

Magnetic tweezers were implemented as described previously (30, 38). The magnet probe used for force applications *in vivo* was built from three rod-shaped strong neodymium magnets (diameter 4 mm; height 10 mm; S-04-10-AN; Supermagnet) prolonged by a sharpened steel piece with a tip radius of ~50 μm to create a magnetic gradient. The surface of the steel tip was electro-coated with gold to prevent oxidation. The probe was controlled with a micromanipulator (Injectman 4, Eppendorf), mounted on an inverted epifluorescent microscope.

Super-paramagnetic particles (diameter 800nm; NanoLink; Solulink) with spontaneous minus end–directed motion were used to apply magnetic forces on the spindles (30, 38). To prepare beads for injection, a solution of 10 μl of undiluted streptavidin-beads was first washed in 100 μL of washing solution (1 M NaCl with 1% Tween-20), and sonicated for 5 min. The beads were then rinsed in 100 μl PBS, incubated 15 min in 100 μl 2 μg/ml Atto565-biotin (Sigma-Aldrich), rinsed again in 100 μl PBS, and finally re-suspended in 20 μl PBS and kept at 4°C until use. Unfertilized eggs were placed on a protamine-coated glass bottom dish. The bead solution was injected using a micro-injection system (FemtoJet 4, Eppendorf) and a micro-manipulator (Injectman 4, Eppendorf). Injection pipettes were prepared from siliconized (Sigmacote) borosilicate glass capillaries (1 mm diameter). Glass capillaries were pulled using a needle puller (P-1000, Sutter Instrument) and ground with a 40° angle on a diamond grinder (EG-40, Narishige) to obtain a 10 μm aperture. Injection pipettes were back-loaded with 2 μl of bead solution before each experiment, and were not re-used. After fertilization, beads were spontaneously transported along MTs and formed a large

aggregate at the center of the aster. This aggregate stayed stably at the centrosome and occasionally split at centrosome duplication. Thus at metaphase, beads sometimes ended up on one or the two spindle poles (Fig S1H and S1I). The targeting of beads towards the centrosomes presumably occurred in a dynein- and microtubule-dependent manner. Thus in the presence of 20 µM Nocodazole or 50 µM Ciliobrevin D, beads could detach from the spindle pole under external forces (Fig S2A and S2B, red arrow heads).

To image spindle displacement and rotation under force, unfertilized eggs stuck on protamine-coated glass dishes were incubated in 10 µg/ml Hoechst (Sigma-Aldrich) and subsequently injected with magnetic beads, and fertilized. At metaphase, chromosomes marked with Hoechst, lined up along the metaphase plate, and the spindle was easily visible as a dumbbell-shaped smooth region in DIC (Differential Interference Contrast), presumably because of its association with the ER (Movie S1). These DIC images allowed to select spindles that were planar and to define the long and short axis directions for force applications. The magnet was then rapidly moved close to the eggs and held at a fixed position either at a position along the spindle axis (for parallel pulls) or orthogonal to the axis for orthogonal pulls (see Movie S2-S3). The end of metaphase was captured as the first time-point when chromosome separated, and the end of anaphase as the first time-point of cleavage furrow ingression. For experiments implicating long force application (Fig 5), the magnet was progressively moved away from the egg using the automatic stage of the microscope.

To actuate oil droplets, unfertilized eggs were placed on protamine-coated glass-bottom dishes. To pull the oil droplets in the cytoplasm, a suspension of 10 µl of 1.2 µm hydrophobic superparamagnetic beads (magtivio, MagSi-proteomics C18) was washed in 100 µl of 30, 50, and 70 percent ethanol solution. It was then dried in vacuum for 20 minutes and re-suspended in 5 µl soybean oil (Naissance; Huile de soja). Preparation of glass capillaries and injection were done with the same methods as for other beads injection described above. All the injected eggs in each sample were surveyed to select the oil droplets with a sufficient amount of beads for pulling. After approaching the magnet, beads inside the oil formed aggregates and slowly moved toward the magnet while the oil droplet was stationary, until the aggregate contacted the oil-cytoplasm interface at the side facing the magnet tip. Large aggregates could not usually cross the interface due the oil surface tension, aggregate size, and hydrophobic properties of the beads, and were used to pull oil droplet in the cytoplasm. Upon force application, the magnet was quickly retracted when the oil distance to the cell cortex was ~10 µm, which caused the aggregate to detach from the oil/cytoplasm interface and the droplet to relaxed backward along the previous pulling force axis (Supplementary Fig 2K and 2L).

Imaging

Time-lapses of spindles and oil droplets moving under magnetic force were recorded on two inverted microscope set-ups equipped with a micromanipulator for magnetic tweezers, at a stabilized room temperature (18–20°C). The first set-up was an inverted epifluorescence microscope (TI-Eclipse, Nikon) combined with a complementary metal–oxide–semiconductor (CMOS) camera (Hamamatsu), using a 20X

dry objective (Apo, NA 0.75, Nikon) and a 1.5X magnifier, yielding a pixel size of 0.216 μm. The second one was a Leica DMI6000 B microscope equipped with an A-Plan 40x/0.65 PH2 objective yielding a pixel size of 0.229 μm, equipped with an ORCA-Flash4.0LT Hamamatsu camera. Both microscopes were operated with Micro-Manager (Open Imaging).

To visualize MTs or bulk F-actin with live probes, live imaging was performed on a spinning-disk confocal microscope (TI-Eclipse, Nikon) equipped with a Yokogawa CSU-X1FW spinning head, and an EM-CCD camera (Hamamatsu), using a 60X water-immersion objective (Apo, NA 1.2, Nikon), equipped with a 3D micromanipulator. Imaging of immunostained cells was performed on a confocal microscope (Zeiss, LSM980) coupled with an Airyscan 2 module in confocal mode with a 63X water immersion objective (NA, 1.4; C-Apo; Zeiss).

Electron Microscopy

Thin sections of eggs fixed as described above were observed by transmission electron microscopy (TEM) at 120 kV with a Tecnai12 transmission electron microscope (Thermo Fischer Scientific) equipped with a 4K Oneview camera (Gatan). For Serial Block Face scanning electron microscopy (SBF-SEM), samples mounted on aluminum pins were trimmed and inserted into a TeneoVS SEM (Thermo Fisher Scientific). Acquisitions were performed with a beam energy of 2.7kV, a current of 400pA, in LowVac mode at 40Pa, a dwell time of 1μs per pixel and sections of 100nm. The pixel size was 20nm.

Magnetic force calibration

Magnetic forces were calibrated *in vitro* following procedures described previously (30, 38). The magnetic force field created by each magnet tip used was first characterized by pulling 2.8 μm mono-dispersed magnetic beads (Dynal) in a viscous test fluid (80% glycerol, viscosity 8.0×10^{-2} Pa sec at 22°C) along the principal axis of the magnet tip. Small motion of the fluid was subtracted by tracking 4 μm non-magnetic tracer fluorescent in the same solution. The speed of a magnetic bead V was computed as a function of the distance to the magnet, representing the decay function of the magnetic force, and fitted using a double exponential function.

To compute the dependence of the force on aggregate size, bead aggregates from the same beads as those used *in vivo* in sizes ranging from 2 to 8 μm, similar to that observed in cells, were pulled in the same fluid as above. The speed V_a was measured and translated into a force using Stokes' law $F=6\pi\eta R V_a$, where η was the viscosity of the test fluid, R the aggregate effective radius defined using the longest length L_1 and the length perpendicular to the longest axis, L_2, as $R=\frac{1}{2}\sqrt{L_1 L_2}$. The force–size relationship at a fixed distance from the magnet was well represented and fitted by a cubic function. These speed–distance and force–size

relationships were combined to compute the magnetic forces applied to spindles inside cells as a function of time, from the size of aggregates at spindle poles and their distance to magnet tips.

Magnetic force calibration for oil droplets experiments followed the exact same procedure as above but establishing the force-size relationships for aggregates of hydrophobic beads used in oil droplets (Fig S2H). In live-cell experiments the sizes of the bead aggregates inside the oil droplets were measured at three different positions in the oil in the bright field, and were averaged.

Analysis of spindle position, orientation, and oil droplets position

Spindle displacement and rotation time-lapses were rotated to align the initial spindle axis to the horizontal X-axis. Magnet tip position was recorded in DIC and the position of bead aggregates were tracked from their fluorescence signal. Spindle position and orientation were processed manually in Fiji by tracking the centers of two smooth disks, which correspond to spindle poles in the DIC channel. This allowed to compute spindle length, center as well as angles with the magnetic force axis. Spindle displacements and magnetic forces were then projected along the horizontal X-axis for parallel pulling or along the Y-axis for orthogonal pulling. Chromosome plate position was also tracked but we often noticed some small delay in the motion of chromosomes as compared to that of spindle poles, presumably caused by some time-scales associated with internal elastic structures that hold chromosomes. Oil droplets were tracked using the TrackMate plugin in Fiji (65) when the contrast was sufficient, and were checked and corrected manually in some cases. Displacement of the oil droplet was corrected when the egg had displaced during the pulling.

Tracking of MT distance to the cortex

Airyscan confocal images stained for MTs and F-actin were projected on a mid-section 2 μm thick, and planar spindles were selected. The horizontal distance between MT ends to the actin cortex was measured, by tracing lines along each MTs to the first border of the F-actin signal using Fiji.

MTs contacting the cortex were also counted from confocal images without F-actin staining in larger z-sections of ~30 μm in thickness and the distance between their ends and the closest surface was measured.

Segmentation of endomembranes from SBF-SEM images

SBF-SEM images were processed using Ilastik a machine-learning-based interactive tool (66). The Pixel classifier was trained iteratively with 3 labels (ER; yolk & mitochondria; cytosol) on a cropped image until a satisfying accuracy was reached for endomembrane compartments. Pixel classification maps were then extracted from the full scale dataset.

Viscoelastic parameter calculation

Spindle displacement and rotation were fitted with a Jeffreys' model using a custom code written in Matlab (Mathworks) to compute viscoelastic parameters. For the rising phase, the spindle position was fitted using:

$$\frac{d(t)}{F(t)} = \frac{1}{\kappa}\left[1 - e^{-\frac{t}{\tau_1}}\right] + \frac{t}{\kappa\tau_2} \, , \qquad\qquad \text{(Equation 1)}$$

where d is the displacement along the X-axis or Y-axis (for parallel or orthogonal pulling respectively), and F is the magnetic force. These fits allowed to compute the restoring stiffness, κ, and the viscoelastic time-scales, τ_1 and τ_2 corresponded to the Jeffreys' viscoelastic timescales, allowing to compute viscous drags on spindles as $\gamma = \kappa\tau_1$

Spindle orientation was fitted similarly, using:

$$\frac{\theta(t)}{T(t)} = \frac{1}{\kappa}\left[1 - e^{-\frac{t}{\tau_1}}\right] + \frac{t}{\kappa\tau_2} \qquad\qquad \text{(Equation 2)}$$

where θ, is the spindle axis angle and T the torque computed as the force projected orthogonal to the spindle long axis and multiplied by half the spindle length. This allowed to compute a rotational stiffness, κ, and viscoelastic time-scales corresponding to rotational behavior under force.

Spindle relaxation dynamics was fitted using:

$$\frac{d(t)}{d(0)} = (1 - a)e^{-\frac{t}{\tau_1}} + a \qquad\qquad \text{(Equation 3)}$$

where t = 0 corresponds to the time of the end of force application, to compute the relaxation offset a and the decay time-scale τ_1. The same equation was used for rotational relaxation but replacing d by θ.

To estimate the enhanced drag of spindles associated with the confinement by the cell boundaries, we used an effective spindle radius defined as: $R_s = \frac{1}{2}\sqrt{L_s W_s}$, where L_s and W_s the length and the width of the spindle. The enhanced drag of a rigid sphere inside a spherical confinement, is computed as $\gamma_c = K\gamma$, were K is a wall correction factor and $\gamma = 6\pi\eta R$ the drag in an infinite medium (50). K is computed as

$$K = \frac{1 - \lambda^5}{1 - \frac{9}{4}\lambda + \frac{5}{2}\lambda^3 - \frac{9}{4}\lambda^5 + \lambda^6} \qquad\qquad \text{(Equation 4)}$$

With λ was the ratio between the spindle radius and that of the egg.

Fit of the data were obtained for each single force experiment, for spindles or oil droplets, using Nonlinear least squares method in Matlab curve fitting. Various combinations of start points of fit parameters were tried and chosen in a way that maximum R-square and tighter confidence interval were achieved. Curves were also visually inspected to ensure that they passed through more points and were not biased with respect to the data points. Finally, other 2 or 3-element models than Jeffreys' were also tested, but failed to provide better fit of all behaviors than this model.

Flow analysis

The recorded spindle pulling images in DIC were analyzed using the particle image velocimetry PIVlab tool in Matlab (67). The exterior of the egg was masked to be excluded from the analysis. Contrast limited adaptive histogram equalization (CLAHE) and two dimensional Wiener filter with accordingly windows of 20 and 3 pixels widths were applied on the images in the pre-processing steps for denoising. Image sequences were investigated in the Fourier space by three interrogation windows with 64, 32, and 16 pixels widths and 50% overlapped area. The spline method was used for the window deformation and subpixel resolution obtained by two-dimensional Gaussian fits. The distribution of the velocity components of the vectors for each set was visually inspected and restricted to remove the outliers in the post-processing stage. Moreover, two other filters based on the standard deviation and local median of velocity vectors were applied to validate the vector fields. The output vector fields after smoothing were used for the analysis. The vector field was temporally averaged over the pulling or relaxation phase except when tracking imaginary tracers.

For measuring the shear rate in the pulling phase, the vector field on the half side of the egg close to the magnet was spatially averaged along the pulling axis (Fig S6B and S6G). Shear rate was calculated as the ratio of the maximum of the velocity component in the direction of pulling divided by the distance taken for the velocity component to drop to zero. Maximums of the velocity components were obtained by a one dimensional Gaussian fits. Spatial autocorrelation in direction was computed as $c(r) = <\hat{s}(r+r_0).\hat{s}(r_0)>$, where $\hat{s}$ and r were the unit vector in the direction of velocity and distance, respectively, and the results were averaged over initial positions r_0. The crossing point of the spatial autocorrelation function with the x axis was considered as the vortex size. Divergence of the vector field was calculated by summation of partial derivatives of its components using central difference. Vorticity was measured as $\omega = \nabla \times v$ where v was the vector field. Vector fields were also used to follow the path of 100 equally spaced tracers along the line perpendicular to the spindle axis by excluding the spindle itself (68). To this aim, the corresponding velocity vector in the selected point was obtained based on bilinear interpolation. The interpolated velocity vector and initial position were used to solve the ordinary differential equation by Euler's method and find the position of the tracer in the next frame. This procedure was continued through all pulling frames.

To compare advection by flows and diffusion, the Peclet number was calculated as Pe=Lu/D with L, u, and D the characteristic length, flow speed, and diffusion coefficient, respectively. Taking the viscosity of the cytoplasm to be 1,000 times that of the water (8), an effective temperature for the active cytoplasm of ~10 times that of room temperature (69), we computed a diffusion coefficient of ~10^{-2} $\mu m^2/s$ for a 1 μm radius vesicle. Measured flow speeds in the cytoplasm was in the order of 10^{-2} $\mu m/s$ and eggs of ~100 μm diameter. This leads to the Peclet number ~10^2 indicating that advection dominates over diffusion for objects of this size.

Statistical analysis

All experiments presented in this MS were repeated at least twice and quantified in a number of cells or events detailed in each figure legend. Statistical and correlation analyses were carried out using Prism 6

20

(GraphPad Software, La Jolla, CA). Statistically significant differences and tests used depended on whether experiments were paired or not and are reported in figure legends.

References

1. K. Luby-Phelps, Cytoarchitecture and physical properties of cytoplasm: volume, viscosity, diffusion, intracellular surface area. *Int Rev Cytol* **192**, 189-221 (2000).

2. K. Luby-Phelps, D. L. Taylor, F. Lanni, Probing the structure of cytoplasm. *J Cell Biol* **102**, 2015-2022 (1986).

3. A. Mogilner, A. Manhart, Intracellular Fluid Mechanics: Coupling Cytoplasmic Flow with Active Cytoskeletal Gel. *Annual Review of Fluid Mechanics* **50**, 347-370 (2018).

4. M. Delarue *et al.*, mTORC1 controls phase separation and the biophysical properties of the cytoplasm by tuning crowding. *Cell* **174**, 338-349. e320 (2018).

5. E. Moeendarbary *et al.*, The cytoplasm of living cells behaves as a poroelastic material. *Nature Materials* **12**, 253-261 (2013).

6. H. Palenzuela *et al.*, In vitro reconstitution of dynein force exertion in a bulk viscous medium. *Current Biology* **30**, 4534-4540. e4537 (2020).

7. F. H. C. Crick, A. F. W. Hughes, The physical properties of cytoplasm: A study by means of the magnetic particle method Part I. Experimental. *Experimental Cell Research* **1**, 37-80 (1950).

8. Y. Hiramoto, Mechanical properties of the protoplasm of the sea urchin egg. II. Fertilized egg. *Exp Cell Res* **56**, 209-218 (1969).

9. Y. Hiramoto, Mechanical properties of the protoplasm of the sea urchin egg. I. Unfertilized egg. *Exp Cell Res* **56**, 201-208 (1969).

10. Y. Tseng, T. P. Kole, D. Wirtz, Micromechanical Mapping of Live Cells by Multiple-Particle-Tracking Microrheology. *Biophysical Journal* **83**, 3162-3176 (2002).

11. M. Guo *et al.*, Probing the stochastic, motor-driven properties of the cytoplasm using force spectrum microscopy. *Cell* **158**, 822-832 (2014).

12. J. Hu *et al.*, Size- and speed-dependent mechanical behavior in living mammalian cytoplasm. *Proc Natl Acad Sci U S A* **114**, 9529-9534 (2017).

13. M. Mittasch *et al.*, Non-invasive perturbations of intracellular flow reveal physical principles of cell organization. *Nat Cell Biol* **20**, 344-351 (2018).

14. B. R. Parry *et al.*, The bacterial cytoplasm has glass-like properties and is fluidized by metabolic activity. *Cell* **156**, 183-194 (2014).

15. R. A. Green, E. Paluch, K. Oegema, Cytokinesis in Animal Cells. *Annual Review of Cell and Developmental Biology* **28**, 29-58 (2012).

16.   N. Minc, M. Piel, Predicting division plane position and orientation. *Trends Cell Biol* **22**, 193-200 (2012).

17.   F. di Pietro, A. Echard, X. Morin, Regulation of mitotic spindle orientation: an integrated view. *EMBO Rep* **17**, 1106-1130 (2016).

18.   Y. Zheng, A membranous spindle matrix orchestrates cell division. *Nat Rev Mol Cell Biol* **11**, 529-535 (2010).

19.   N. Schweizer, N. Pawar, M. Weiss, H. Maiato, An organelle-exclusion envelope assists mitosis and underlies distinct molecular crowding in the spindle region. *J Cell Biol* **210**, 695-704 (2015).

20.   M. Schuh, J. Ellenberg, A new model for asymmetric spindle positioning in mouse oocytes. *Curr Biol* **18**, 1986-1992 (2008).

21.   J. Azoury *et al.*, Spindle positioning in mouse oocytes relies on a dynamic meshwork of actin filaments. *Curr Biol* **18**, 1514-1519 (2008).

22.   S. W. Grill, J. Howard, E. Schaffer, E. H. Stelzer, A. A. Hyman, The distribution of active force generators controls mitotic spindle position. *Science* **301**, 518-521 (2003).

23.   A. Haupt, N. Minc, How cells sense their own shape - mechanisms to probe cell geometry and their implications in cellular organization and function. *J Cell Sci* **131** (2018).

24.   M. Dogterom, J. W. Kerssemakers, G. Romet-Lemonne, M. E. Janson, Force generation by dynamic microtubules. *Curr Opin Cell Biol* **17**, 67-74 (2005).

25.   J. Howard, Elastic and damping forces generated by confined arrays of dynamic microtubules. *Phys Biol* **3**, 54-66 (2006).

26.   I. M. Tolic-Norrelykke, Push-me-pull-you: how microtubules organize the cell interior. *Eur Biophys J* **37**, 1271-1278 (2008).

27.   J. Howard, C. Garzon-Coral, Physical Limits on the Precision of Mitotic Spindle Positioning by Microtubule Pushing forces: Mechanics of mitotic spindle positioning. *Bioessays* **39** (2017).

28.   C. Garzon-Coral, H. A. Fantana, J. Howard, A force-generating machinery maintains the spindle at the cell center during mitosis. *Science* **352**, 1124-1127 (2016).

29.   N. Ierushalmi *et al.*, Centering and symmetry breaking in confined contracting actomyosin networks. *Elife* **9** (2020).

30.   J. Salle *et al.*, Asymmetric division through a reduction of microtubule centering forces. *The Journal of cell biology* **218**, 771-782 (2019).

31.   T. Kiyomitsu, I. M. Cheeseman, Cortical dynein and asymmetric membrane elongation coordinately position the spindle in anaphase. *Cell* **154**, 391-402 (2013).

32.   N. Minc, D. Burgess, F. Chang, Influence of cell geometry on division-plane positioning. *Cell* **144**, 414-426 (2011).

33.   T. Mitchison *et al.*, Growth, interaction, and positioning of microtubule asters in extremely large vertebrate embryo cells. *Cytoskeleton (Hoboken)* **69**, 738-750 (2012).

34.   M. Wühr *et al.*, Evidence for an Upper Limit to Mitotic Spindle Length. *Current Biology* **18**, 1256-1261 (2008).

35.   V. E. Foe, G. von Dassow, Stable and dynamic microtubules coordinately shape the myosin activation zone during cytokinetic furrow formation. *J Cell Biol* **183**, 457-470 (2008).

36.   A. Spudich, J. T. Wrenn, N. K. Wessells, Unfertilized sea urchin eggs contain a discrete cortical shell of actin that is subdivided into two organizational states. *Cell Motil Cytoskeleton* **9**, 85-96 (1988).

37.   C. F. Asnes, T. E. Schroeder, Cell cleavage. Ultrastructural evidence against equatorial stimulation by aster microtubules. *Exp Cell Res* **122**, 327-338 (1979).

38.   H. Tanimoto, J. Salle, L. Dodin, N. Minc, Physical Forces Determining the Persistency and Centering Precision of Microtubule Asters. *Nat Phys* **14**, 848-854 (2018).

39.   A. Colin *et al.*, Active diffusion in oocytes nonspecifically centers large objects during prophase I and meiosis I. *J Cell Biol* **219** (2020).

40.   J. F. Pelletier, C. M. Field, S. Furthauer, M. Sonnett, T. J. Mitchison, Co-movement of astral microtubules, organelles and F-actin by dynein and actomyosin forces in frog egg cytoplasm. *Elife* **9** (2020).

41.   H. Wang *et al.*, Symmetry breaking in hydrodynamic forces drives meiotic spindle rotation in mammalian oocytes. *Sci Adv* **6**, eaaz5004 (2020).

42.   J. G. Carlton, H. Jones, U. S. Eggert, Membrane and organelle dynamics during cell division. *Nat Rev Mol Cell Biol* **21**, 151-166 (2020).

43.   H. A. Barnes, J. F. Hutton, K. Walters, *An introduction to rheology* (Elsevier, 1989), vol. 3.

44.   H. Frohlich, R. Sack, Theory of the rheological properties of dispersions. *Proc R Soc Lond A Math Phys Sci* **185**, 415-430 (1946).

45.   R. B. Bird, R. C. Armstrong, O. Hassager, Dynamics of polymeric liquids. Vol. 1: Fluid mechanics. (1987).

46.   J. Howard, Ed., *Mechanics of Motor Proteins and the Cytoskeleton* (Sinauer Associates, Inc, 2001).

47.   M. T. Valentine, Z. E. Perlman, T. J. Mitchison, D. A. Weitz, Mechanical properties of Xenopus egg cytoplasmic extracts. *Biophys J* **88**, 680-689 (2005).

48. E. Nazockdast, A. Rahimian, D. Needleman, M. Shelley, Cytoplasmic flows as signatures for the mechanics of mitotic positioning. *Mol Biol Cell* **28**, 3261-3270 (2017).

49. A. De Simone, A. Spahr, C. Busso, P. Gonczy, Uncovering the balance of forces driving microtubule aster migration in C. elegans zygotes. *Nat Commun* **9**, 938 (2018).

50. J. Happel, H. Brenner, *Low Reynolds number hydrodynamics: with special applications to particulate media* (Springer Science & Business Media, 2012), vol. 1.

51. R. B. Nicklas, Measurements of the force produced by the mitotic spindle in anaphase. *The Journal of cell biology* **97**, 542-548 (1983).

52. S. W. Grill, P. Gonczy, E. H. Stelzer, A. A. Hyman, Polarity controls forces governing asymmetric spindle positioning in the Caenorhabditis elegans embryo. *Nature* **409**, 630-633 (2001).

53. D. T. Bergstralh, D. St Johnston, Spindle orientation: what if it goes wrong? *Semin Cell Dev Biol* **34**, 140-145 (2014).

54. M. E. Larson, W. M. Bement, Automated mitotic spindle tracking suggests a link between spindle dynamics, spindle orientation, and anaphase onset in epithelial cells. *Mol Biol Cell* **28**, 746-759 (2017).

55. Z. Tang *et al.*, Mechanical Forces Program the Orientation of Cell Division during Airway Tube Morphogenesis. *Dev Cell* **44**, 313-325 e315 (2018).

56. T. J. Mitchison, K. Ishihara, P. Nguyen, M. Wuhr, Size Scaling of Microtubule Assemblies in Early Xenopus Embryos. *Cold Spring Harb Perspect Biol* **7**, a019182 (2015).

57. A. Chaigne *et al.*, F-actin mechanics control spindle centring in the mouse zygote. *Nat Commun* **7**, 10253 (2016).

58. O. M. Lancaster *et al.*, Mitotic rounding alters cell geometry to ensure efficient bipolar spindle formation. *Dev Cell* **25**, 270-283 (2013).

59. N. R. Stevens, A. A. Raposo, R. Basto, D. St Johnston, J. W. Raff, From stem cell to embryo without centrioles. *Curr Biol* **17**, 1498-1503 (2007).

60. A. Khodjakov, R. W. Cole, B. R. Oakley, C. L. Rieder, Centrosome-independent mitotic spindle formation in vertebrates. *Curr Biol* **10**, 59-67 (2000).

61. L. Carlini, G. P. Brittingham, L. J. Holt, T. M. Kapoor, Microtubules Enhance Mesoscale Effective Diffusivity in the Crowded Metaphase Cytoplasm. *Dev Cell* **54**, 574-582 e574 (2020).

62. T. Mitchison, G. Charras, L. Mahadevan (2008) Implications of a poroelastic cytoplasm for the dynamics of animal cell shape. in *Seminars in cell & developmental biology* (Elsevier), pp 215-223.

63. Y. Shimamoto, Y. T. Maeda, S. Ishiwata, A. J. Libchaber, T. M. Kapoor, Insights into the micromechanical properties of the metaphase spindle. *Cell* **145**, 1062-1074 (2011).

64. P. Bun, S. Dmitrieff, J. M. Belmonte, F. J. Nedelec, P. Lenart, A disassembly-driven mechanism explains F-actin-mediated chromosome transport in starfish oocytes. *Elife* **7** (2018).

65. J. Y. Tinevez *et al.*, TrackMate: An open and extensible platform for single-particle tracking. *Methods* **115**, 80-90 (2017).

66. S. Berg *et al.*, ilastik: interactive machine learning for (bio)image analysis. *Nat Methods* **16**, 1226-1232 (2019).

67. W. Thielicke, E. J. Stamhuis, PIVlab – Towards User-friendly, Affordable and Accurate Digital Particle Image Velocimetry in MATLAB. *Journal of Open Research Software* **2** (2014).

68. H. P. Zhang, A. Be'er, R. S. Smith, E. L. Florin, H. L. Swinney, Swarming dynamics in bacterial colonies. *EPL (Europhysics Letters)* **87**, 48011 (2009).

69. H. E. Egelman, *Comprehensive Biophysics*. H. E. Egelman, Ed. (Elsevier 2012).
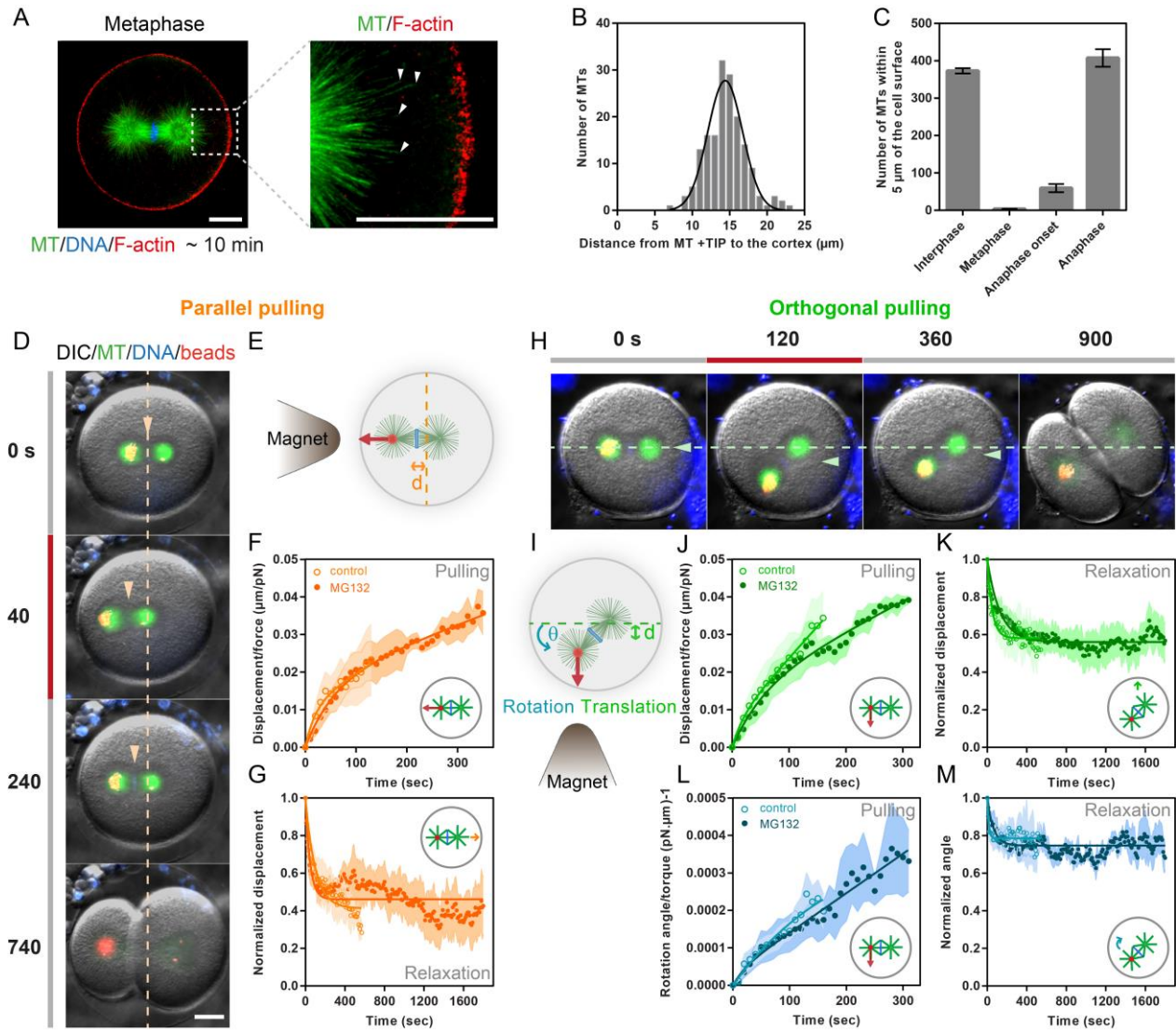
Figure 1. Viscoelastic forces hold spindles in the center of large cells even in the absence of astral Microtubules contacting the cell cortex. (A) (Left) Airy-scan confocal image of a sea urchin zygote in metaphase fixed and stained for Microtubules (MTs), DNA and F-actin. (Right) Close up view on + Ends of microtubules, marked with white arrowheads, and the actin-rich cortex. **(B)** Quantification of the distance from MT+ TIPS to the actin cortex (n= 168 MTs from 4 eggs). **(C)** Number of MTs reaching a distance less than 5 μm from the cortex in different phase of the first cell cycle (n= 3, 20, 5 and 2 cells respectively). Error bars correspond to +/- SEM. **(D-E)** Time-lapse of metaphase spindles with magnetic beads bound to one spindle pole, displaced by magnetic forces applied parallel to the spindle axis by the presence of a magnet tip, and recoiling upon force cessation. **(F)** Time evolution of the displacement measured from the initial centered position of the spindle normalized by the applied force for metaphase spindles in normal cells (n=11) and in cells treated with MG132 to arrest cells in metaphase (n=9). **(G)** Time evolution of the displacement back to the cell center when the external force is released, normalized to that at the moment of force cessation, for the same cells and conditions as in F. **(H-I)** Time-lapse of metaphase spindles displaced and rotated by magnetic forces applied orthogonal to the spindle axis, and spindle recoiling upon force cessation. **(J)** Time evolution of the displacement measured from the initial centered position of the spindle and normalized by the applied force in normal cells (n=14) and in cells treated with MG132 (n=7). **(K)** Time evolution of the normalized displacement back to the cell center when the external force is released for the same cells and conditions as in J. **(L)** Time evolution of the spindle axis angle normalized by the external torque applied in normal cells (n=14) and in cells treated with MG132 (n=7). **(M)** Time evolution of the normalized angle when the external torque is released for the same cells and conditions as in L. In F-G, and J-M, the bold lines correspond to fits of the data using general creep or relaxation equations of the Jeffreys' viscoelastic model (see main text and methods). Error bars are represented as shades in these curves and correspond to +/- S.D/2. Scale bars, 20 μm.
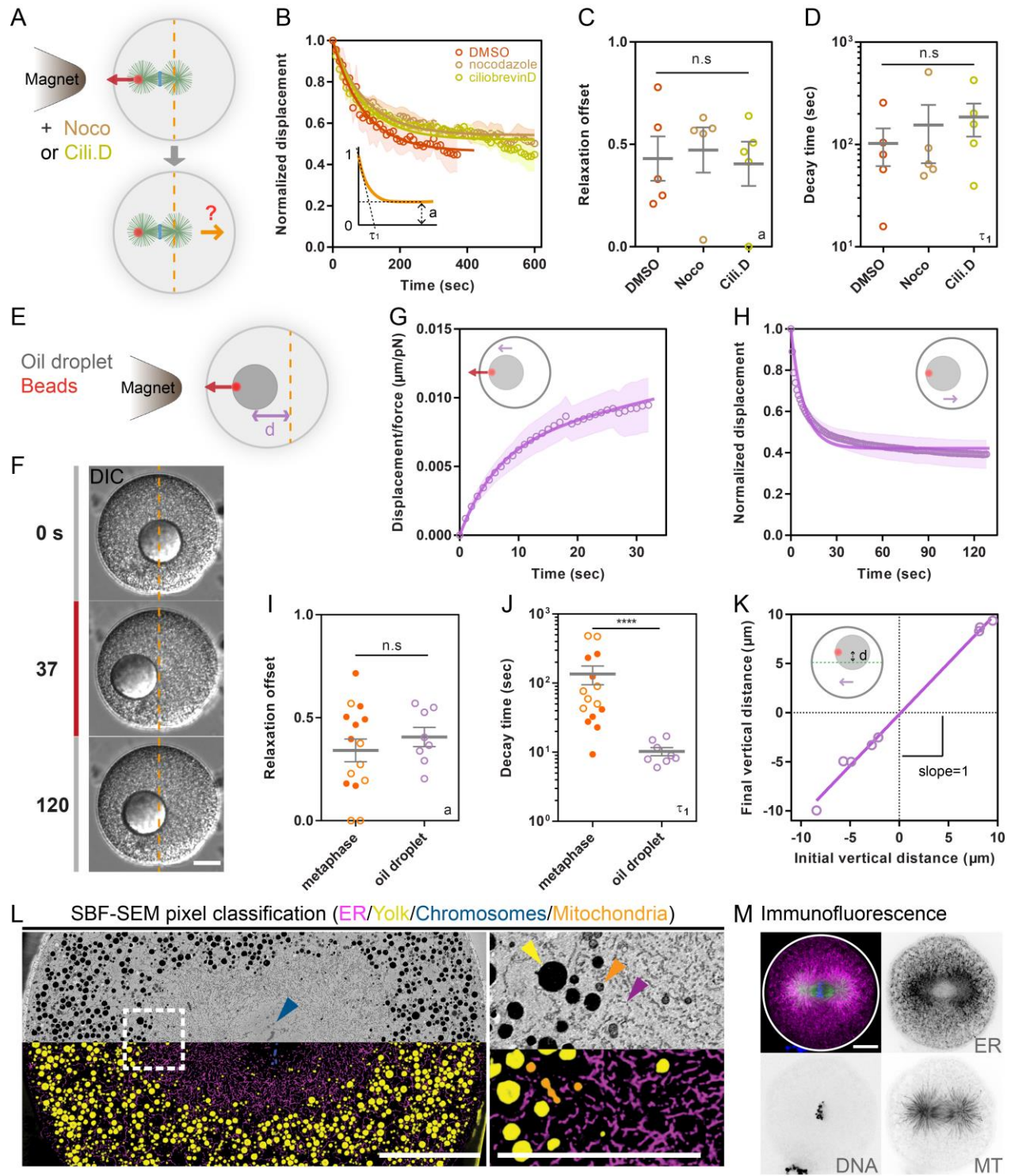
Figure 2. Visco-elastic restoring forces on spindles are associated to the material properties of bulk cytoplasm. (A-B) Metaphase spindles are displaced with magnetic tweezers and treated with either DMSO as controls (n=5), Nocodazole to affect microtubules (n=5 cells) or Ciliobrevin D to inhibit Dynein activity (n=5 cells), and their recoiling behavior to the cell center is assayed. **(C-D)** Quantification of the positional offsets to the cell center, a, and decay time-scales τ_1 of relaxation curves plotted in B, using a single exponential model as indicated in the inset in B. **(E)** Scheme representing injected oil droplets containing hydrophobic magnetic beads used to actuate large objects with magnetic tweezers in the cytoplasm. **(F)** Time-lapse of a magnetic oil droplet displaced with an external magnetic force and recoiling upon force cessation. **(G)** Time evolution of the displacement measured from the initial position of the droplet and normalized by the applied force (n=5 cells). **(H)** Time evolution of the normalized displacement of the droplet back to its initial position upon force cessation. **(I-J)** Relaxation offset and decay time-scales for metaphase spindles (n=15) and oil droplets (n=8). **(K)** Final vertical offset plotted as a function of the initial vertical offset for droplets displaced horizontally with magnetic tweezers and let to relax (n=8). The line is a linear fit with a slope of 1.04. **(L)** Mid-section of a fixed metaphase zygote imaged with serial block face scanning electron microscopy (SBF-SEM) and corresponding pixel classification of different endomembrane compartments in the cytoplasm, and close up view at the border between the spindle and the rest of the cytoplasm. **(M)** Projected spinning disk confocal image of a metaphase zygote fixed and stained for Microtubules, DNA and Endoplasmic reticulum. Error bars and shades represent +/- S.E.M and +/- S.D/2 respectively. Results were compared using a two-tailed Mann–Whitney test. n.s, $P > 0.05$, ****, $P < 0.0001$. Scale bars, 20 µm and 10 µm in the close up view of 2L.
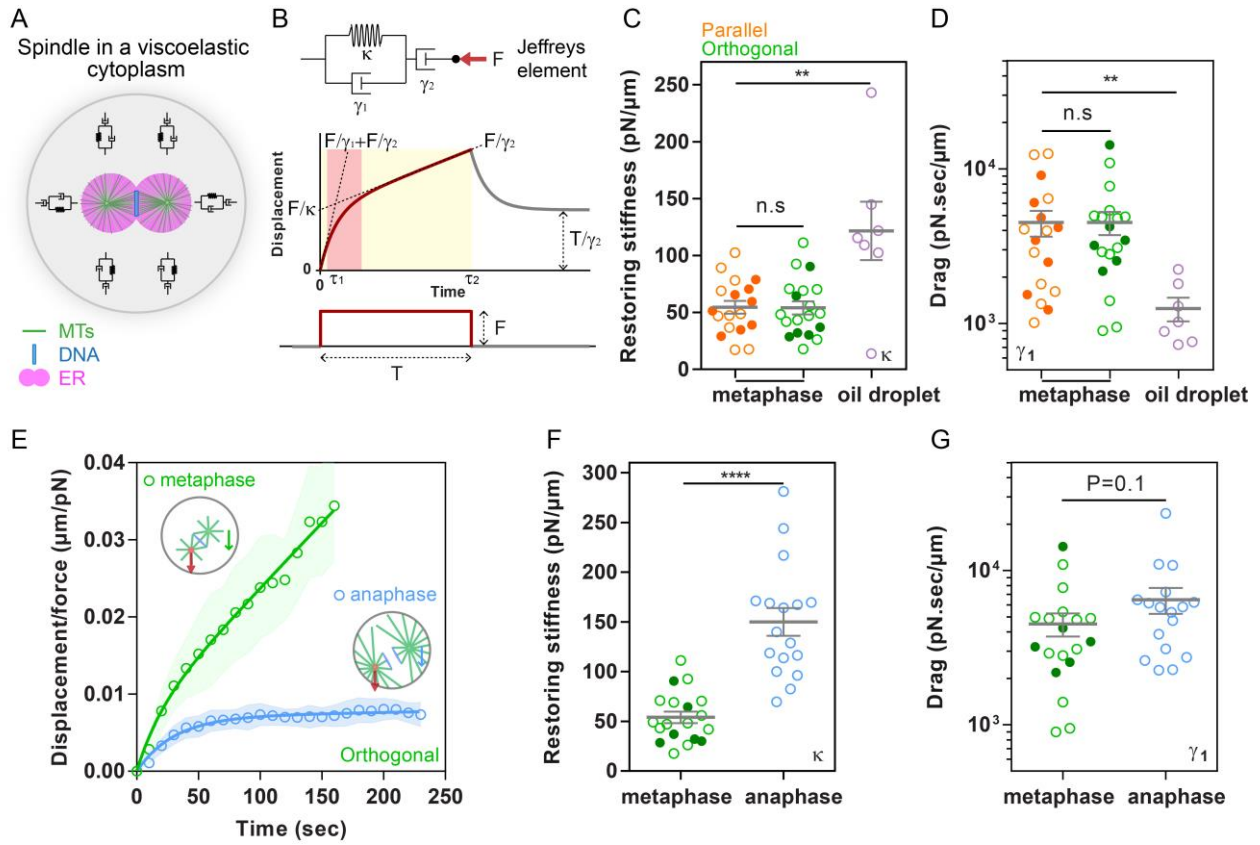
Figure 3. Cytoplasm material generates large elastic and viscous drags on mitotic spindles of similar magnitude as those applied by active microtubule arrays. (A) Scheme of metaphase spindles held in the cell center by viscoelastic elements in the cytoplasm. **(B)** Scheme of Jeffreys 3-element model made of a spring and a dashpot in parallel and another dashpot in series, and typical creep and relaxation behavior of this element. **(C-D)** Cytoplasm restoring stiffness and viscous drags on mitotic spindles moved parallel or orthogonal to the spindle axis (n= 18 and 19 respectively) and for oil droplets (n=7), computed using fits to the Jeffreys' models represented in B. Open and closed dots correspond respectively to data obtained in control or MG132 treated cells. **(E)** Time evolution of the displacement measured from the initial centered position of the spindle and normalized by the applied force in metaphase and anaphase. **(F-G)** Restoring stiffness and viscous drags of metaphase and anaphase spindles moved orthogonal to the spindle axis (n=19 and 17 respectively). Error bars and shades correspond to +/- S.E.M and +/- S.D/2 respectively. Results were compared by using a two-tailed Mann–Whitney test. n.s, $P > 0.05$, **, $P < 0.01$, ****, $P < 0.0001$.
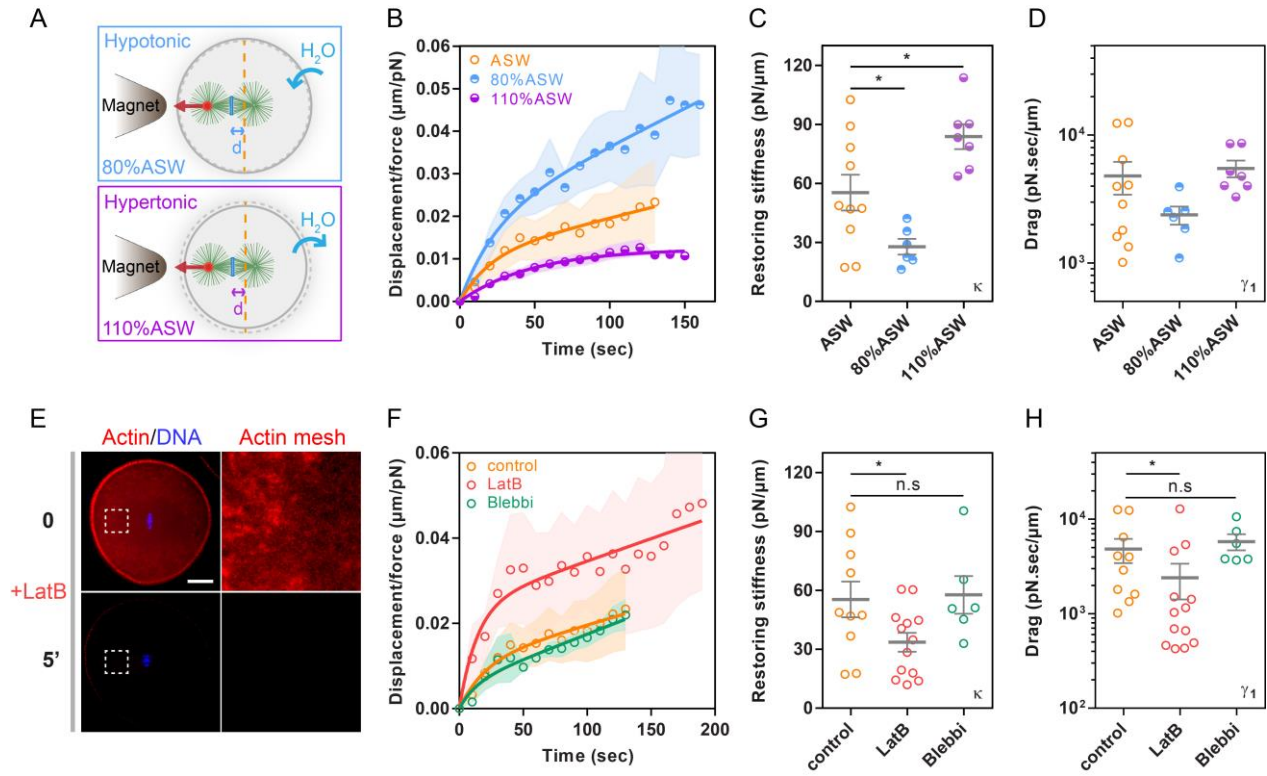
Figure 4. Influence of cytoplasm crowding and F-actin meshwork on spindle restoring stiffness and drags. (A) Scheme representing experiments to change cytoplasmic density by placing eggs in hypotonic or hypertonic artificial sea water (ASW). **(B)** Displacement normalized by applied force of metaphase spindles in control (n=10), hypotonic (n=6) and hypertonic (n=7) sea water. **(C-D)** Cytoplasm resorting stiffness and viscous drags on mitotic spindles moved parallel to the spindle axis, in controls, hypotonic or hypertonic sea water. **(E)** Confocal images of eggs injected with Utrophin-488 to visualize F-actin at metaphase in bulk cytoplasm (top) and ~5 min after treating the same cell with Latrunculin B (bottom). The two images are treated with the same contrast to compare F-actin signals. **(F)** Displacement normalized by applied force of metaphase spindles in control (n=10), cells treated with Latrunculin B (n=13) and cells treated with Blebbistatin (n=6). **(G-H)** Cytoplasm restoring stiffness and viscous drags in controls, cells treated with Latrunculin B and cells treated with Blebbistatin. Error bars and shades correspond to +/- S.E.M and +/- S.D/2 respectively. Results were compared by using a two-tailed Mann–Whitney test. n.s, $P > 0.05$, *, $P < 0.05$. Scale bars, 20 μm.
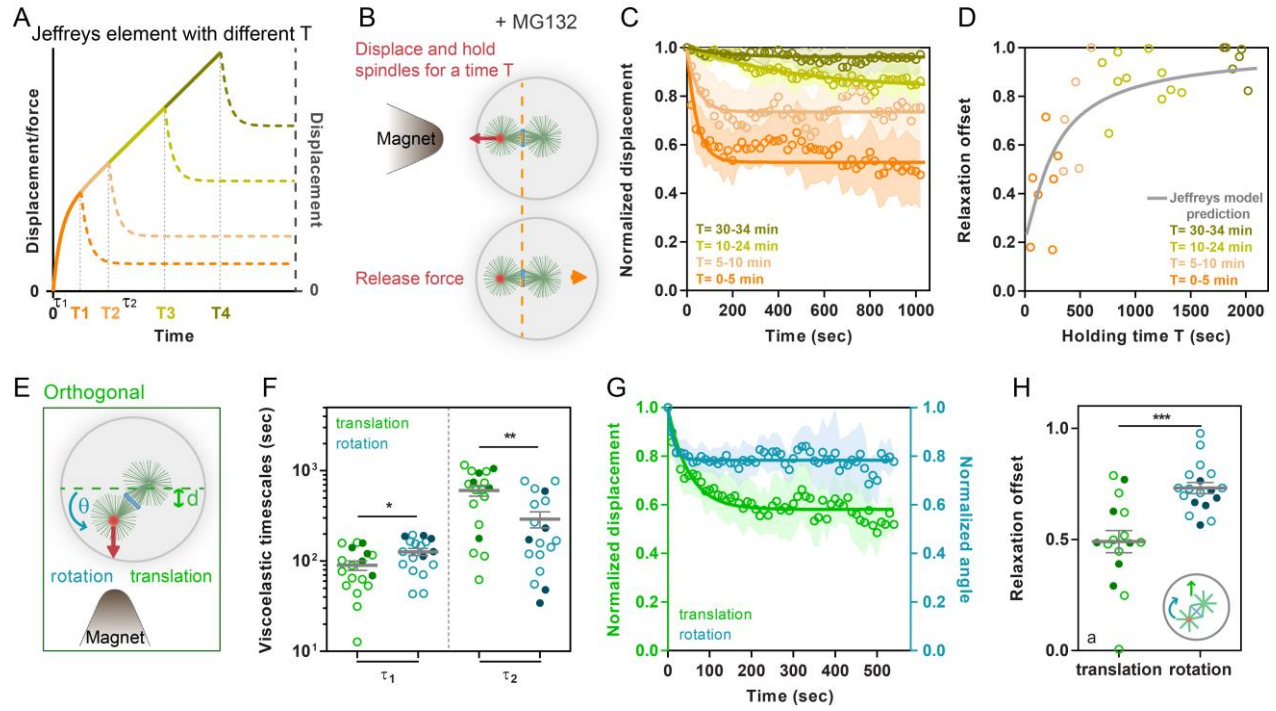
Figure 5. Dissipation of stored elastic energy and implications for asymmetric and oriented divisions. (A) Theoretical curve of creep and relaxation curves for different force application times in the Jeffreys' model. Note how longer force applications tend to dissipate positional memory during relaxation. **(B)** Scheme explaining the assay to test the influence of force application time on relaxation. **(C)** Relaxation responses of metaphase spindles pulled and held with magnetic tweezers for increasing durations. **(D)** Relaxation offset, *a,* plotted as a function of force application duration, overlaid with the predicted theoretical curve form Jeffreys' model, $a = \frac{1}{1+\frac{\tau_2}{T}(1-e^{-T/\tau_1})}$, using measured values of τ_1 and τ_2. **(E)** Scheme representing how spindle rotation and displacement can be compared in the orthogonal pulling assay. **(F)** Viscoelastic time-scales τ_1 and τ_2 for rotational and translational spindle motions under force for the same cells and spindles (n=18). Open and closed dots correspond respectively to data obtained in control or MG132 treated cells. **(G)** Rotational and translational relaxation curves upon force cessation. **(H)** Relaxation offset for rotational and translational relaxation. Error bars and shades correspond to +/- S.E.M and +/- S.D/2 respectively. Results were compared by using a two-tailed Wilcoxon test. *, P < 0.05, **, P < 0.01, ***, P < 0.001.
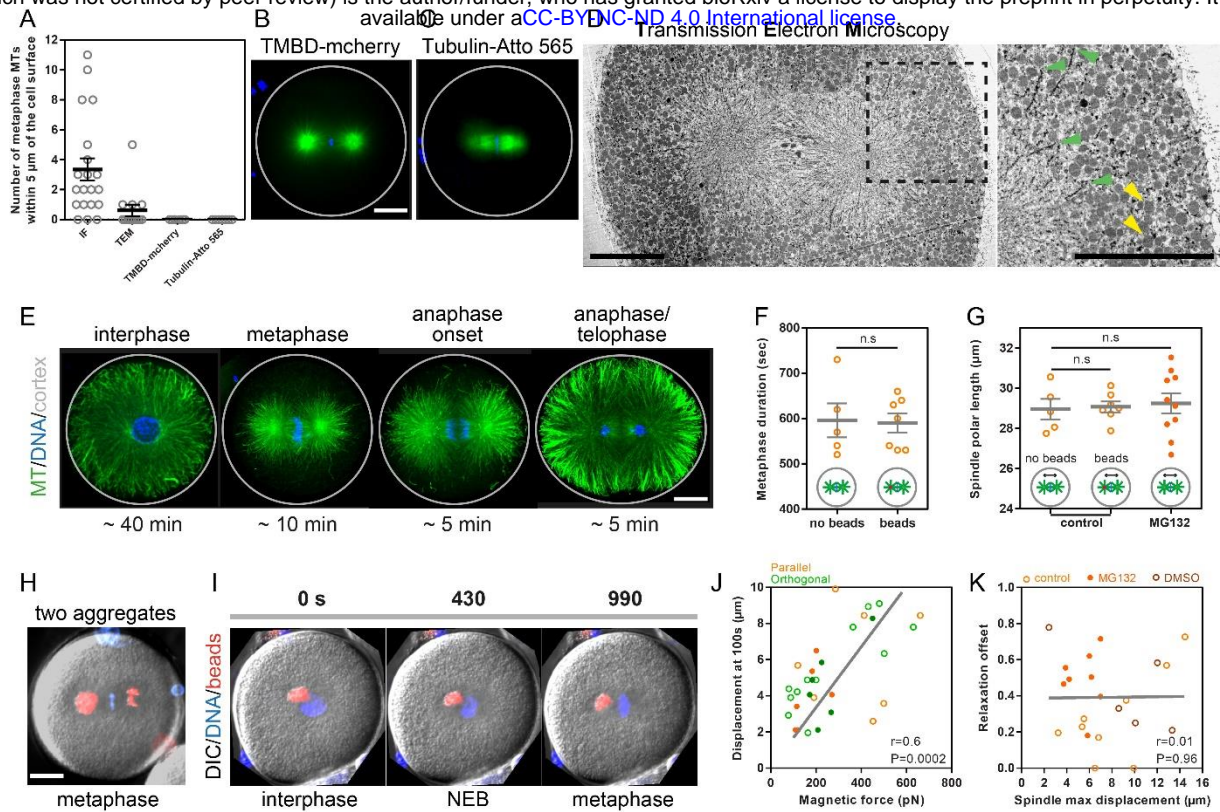
36
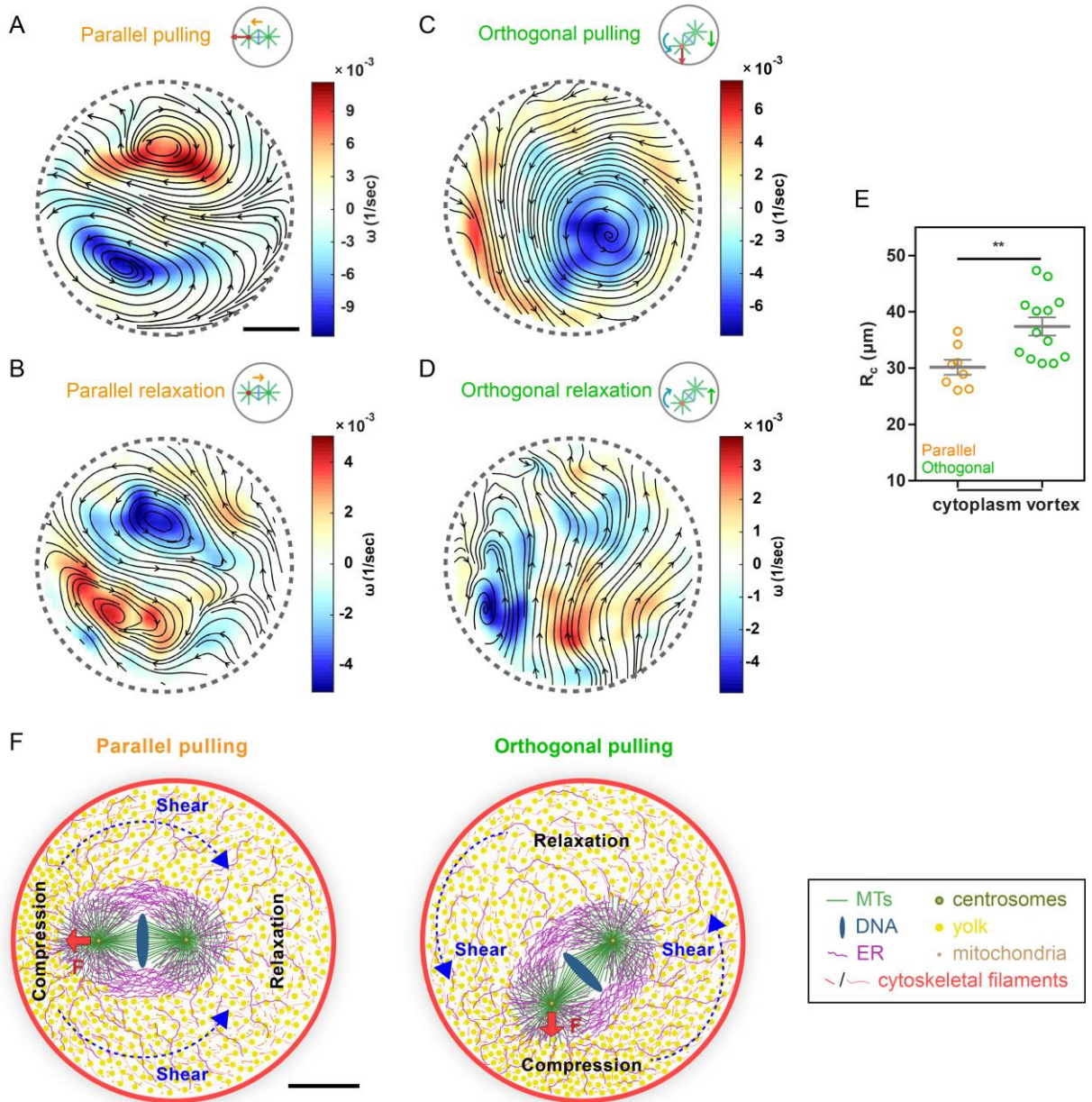
Figure 6. Large-scale flows of cytoplasm elements associated with spindle motions. (A-D) Cytoplasm streamlines averaged on a duration of 60 s and size of 50 μm during parallel force application on spindles (A) and during spindle recoils (B), or during orthogonal force applications averaged on a duration of 100 s and size of 90 μm (C) and relaxation (D). Streamlines are superimposed onto a color map of local flow vorticities, ω. **(E)** Quantification of flow vortices size during parallel or orthogonal pulls   (n=8 and 13 cells respectively). **(F)** Proposed models based on flow map analysis and force response of metaphase spindles. In parallel pulls, the cytoplasm matrix made of relatively large objects including cytoskeletal elements and endomembranes (Yolk, mitochondria or ER), is compressed at the spindle front and stretched at the rear, which causes it to push or pull back the spindle with elastic restoring forces. At the same time, this matrix is sheared along the spindle. In orthogonal pulls, compression of the cytoplasm may be prominent at the spindle front, like in parallel pulls, but in rotation, the broken symmetry causes shear to dominate over compression. Shear stresses fluidize or plastically rearrange the cytoplasm faster than in compression potentially accounting for reduced elastic restoring of spindle angles as compared to positions upon force applications. Results were compared by using a two-tailed Mann–Whitney test. **, $P < 0.01$. Scale bars, 20 μm.

SUPPORTING INFORMATION

This supporting information file contains 6 Supplemental Figures and Figure Legends and supporting

movie legends.

A — Number of metaphase MTs within 5 μm of the cell surface: IF, TEM, TMBD-mcherry, Tubulin-Atto 565

B — TMBD-mcherry, Tubulin-Atto 565

D — Transmission Electron Microscopy

E — MT/DNA/cortex: interphase (~ 40 min), metaphase (~ 10 min), anaphase onset (~ 5 min), anaphase/telophase (~ 5 min)

F — Metaphase duration (sec): no beads, beads; n.s

G — Spindle polar length (μm): no beads, beads (control), MG132; n.s, n.s

H — two aggregates; metaphase

I — DIC/DNA/beads: 0 s (interphase), 430 (NEB), 990 (metaphase)

J — Displacement at 100s (μm) vs Magnetic force (pN); Parallel, Orthogonal; r=0.6, P=0.0002

K — Relaxation offset vs Spindle max displacement (μm); control, MG132, DMSO; r=0.01, P=0.96

Figure S1. Metaphase astral MTs do not reach the cortex, yet spindles can recoil back to the cell center upon force-induced displacement. (A) Number of astral MTs reaching a distance less than 5μm to the cortex in metaphase as assayed by Immunofluorescence (IF), Transmission electron microscopy (TEM), or live-imaging of injected TMBD-mCherry or Tublin-Atto-565. **(B-C)** Representative images of metaphase spindles in live cells with MTs labelled by injecting the indicated probes. **(D)** Transmission electron microscopy using fixation methods to reveal the presence of MTs, and close up view with green arrowheads pointing at MT + TIPs, and yellow arrowheads pointing at yolk granules. **(E)** Immunofluorescence of MTs imaged with confocal microscopy in different indicated phases of the cell cycle. The time below the images correspond to the average duration of the cell cycle phases. **(F)** Duration of metaphase in normal zygotes and in zygotes injected with magnetic beads that attach to mitotic spindles. **(G)** Spindle polar length in controls, cells injected with magnetic beads or in cells treated with MG132. **(H)** Example image of an egg in which bead aggregates have split and accumulated on the two spindle poles. **(I)** Time-sequence of a bead aggregate that accumulates at one spindle pole from interphase to metaphase. **(J)** Displacement after 100s of force application plotted as a function of the applied force for both orthogonal and parallel pulls (n=32). The line is a linear fit, and correlation coefficients and corresponding P-values are indicated in the plot. **(K)** Relaxation offset during spindle recoils is independent of the distance of the spindle to the cortex. The line is a linear fit, and correlation coefficients and corresponding P-values indicated in the plot**.** Error bars correspond to +/- S.E.M. Results were compared by using a two-tailed Mann–Whitney test. n.s, P > 0.05.
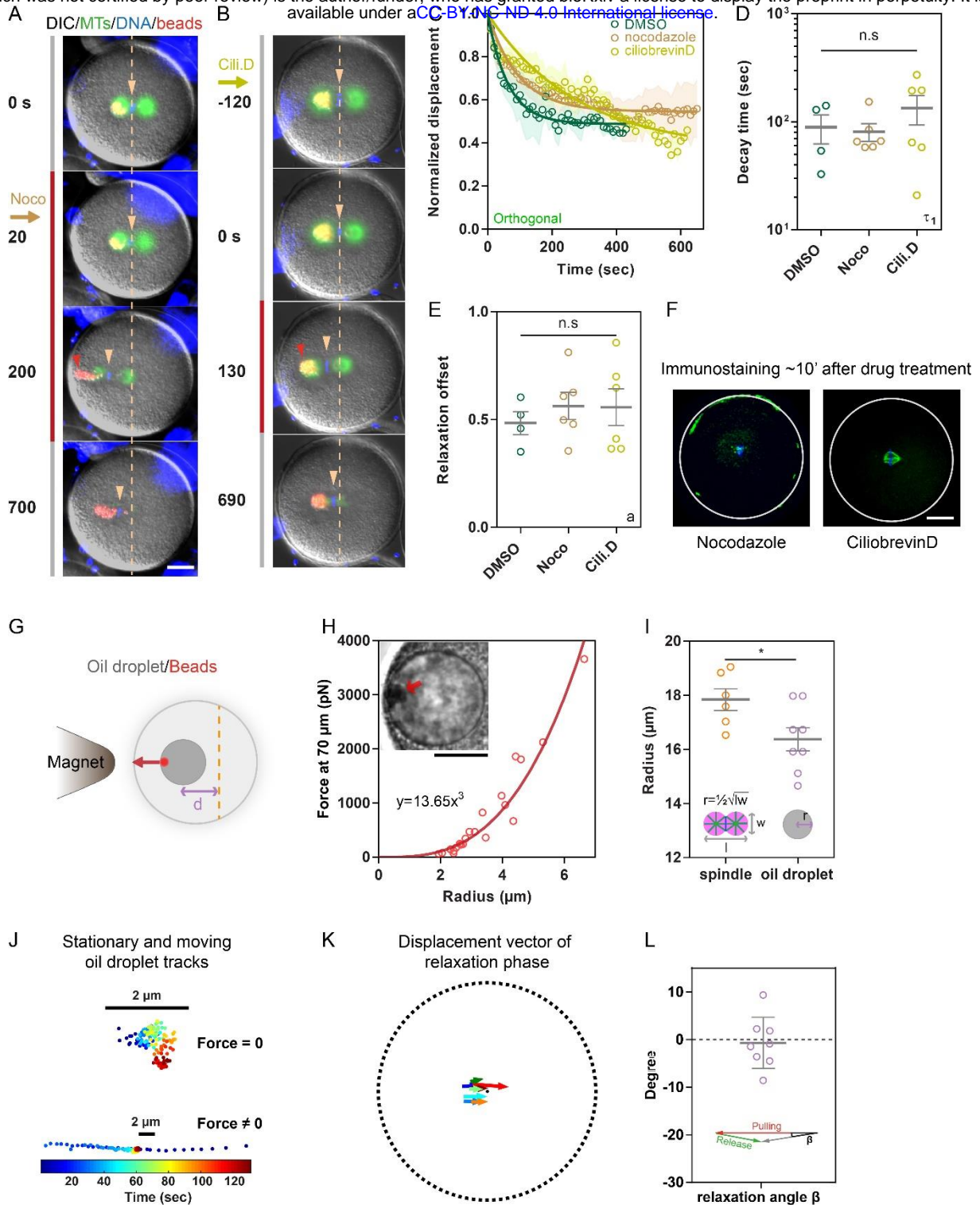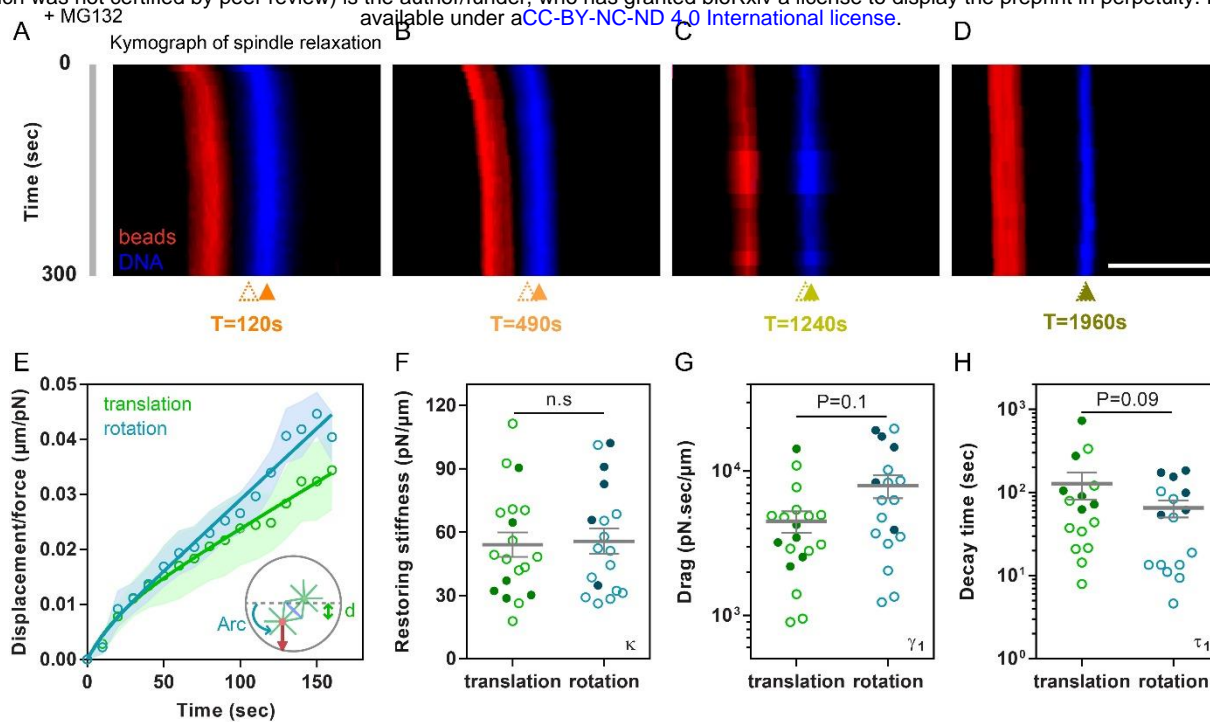
Figure S2. Viscoelastic spindle recoils are independent of MTs and dynein, and occur with similar characteristics for a passive oil droplet. (A) Time-lapse of a spindle pulled with magnetic tweezers and treated during the pull with Nocodazole to depolymerize MTs, and monitor recoils in the absence of MTs. Note the disappearance of MTs. **(B)** Egg treated with Ciliobrevin D to inhibit dynein activity and pulled and let to recoil. Note the progressive shrinking of the spindle caused by dynein inhibition. In these two sets of experiments the drugs were added at different timings to ensure that the effect was maximum at the end of the pulling phase, based on multiple optimization assays (see Methods). **(C)** Time evolution of the normalized displacement back to the cell center in orthogonal pulls when the external force is released in cells treated with the indicated chemicals (n=4 for DMSO, 6 for Nocodazole, 6 for Ciliobrevin D). **(D-E)** Quantification of the positional offsets to the cell center, and decay time-scales of relaxation curves plotted in C, using a single exponential model. **(F)** Confocal images of zygotes after treatment of indicated chemicals. **(G)** Scheme of the assay used to move magnetized oil droplets in cells with magnetic tweezers. **(H)** Close up view of hydrophobic beads aggregates within oil droplets, used to quantify the size of the aggregates, and calibration curve linking the force at 70 µm from the magnet tip to the center of the aggregate. **(I)** Quantification of spindle (n=6) and oil droplets sizes (n=8). **(J)** Tracking of oil droplet centers in the absence and in the presence of external forces. **(K)** Displacement vectors of oil droplets center during the relaxation after force cessation. **(L)** Quantification of the deviation angle between the pulling and relaxation trajectories in individual magnetic oil droplets experiments (n=8). Error bars and shades correspond to +/- S.E.M and +/- S.D/2 respectively. Results were compared by using a two-tailed Mann–Whitney test. n.s, P > 0.05, *, P < 0.05. Scale bars, 20 µm, unless otherwise indicated.
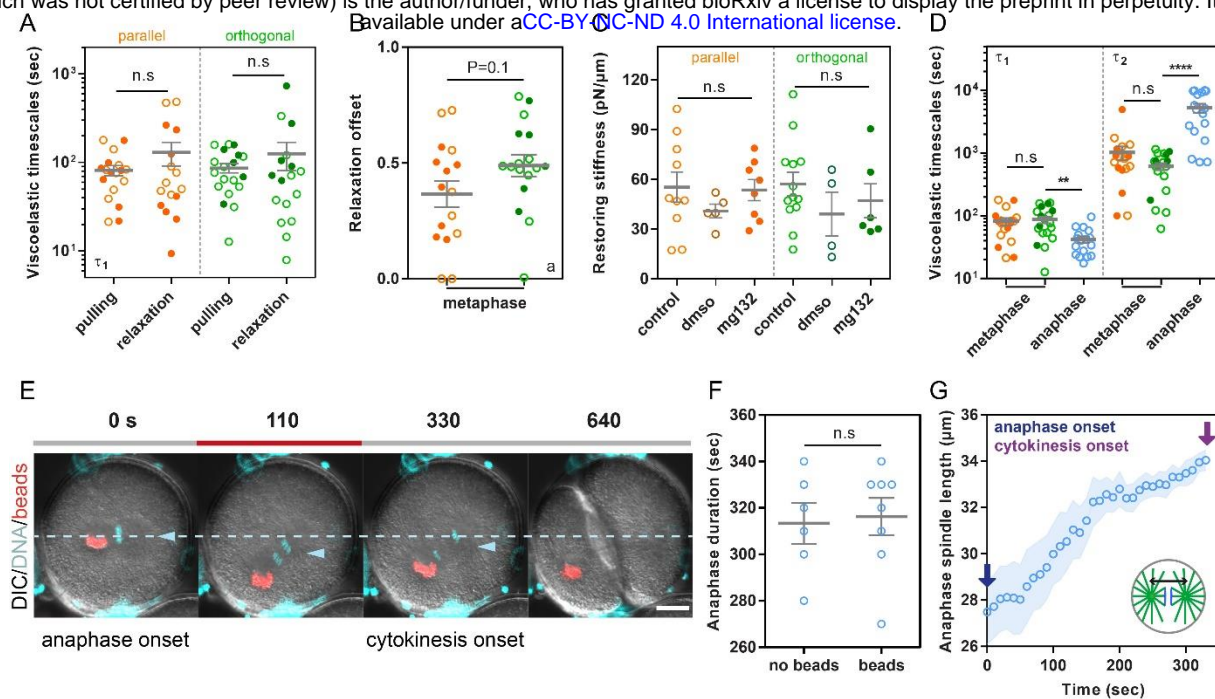
Figure S3. Comparison of metaphase and anaphase spindles pulls and relaxation. (A) Viscoelastic timescales, τ_1 measured during the rising pulling phase or the relaxation phase. **(B)** Relaxation offsets for metaphase spindles pulled parallel or orthogonal. **(C)** Restoring stiffness measured for the indicated conditions in parallel and orthogonal pulls. **(D)** Viscoelastic time-scales for metaphase (n=18 for parallel and 19 for orthogonal pulls) and anaphase spindles pulls (n=17). **(E)** Time-lapse of a representative pulling and relaxing experiment on anaphase spindles. **(F)** Anaphase duration for control eggs vs eggs injected with magnetic beads. **(G)** Time-evolution of anaphase spindle length. Error bars and shades correspond to +/- S.E.M and +/- S.D/2 respectively. Results were compared by using a two-tailed Mann–Whitney test. n.s, $P > 0.05$, **, $P < 0.01$, ****, $P < 0.0001$. Scale bars, 20 µm.
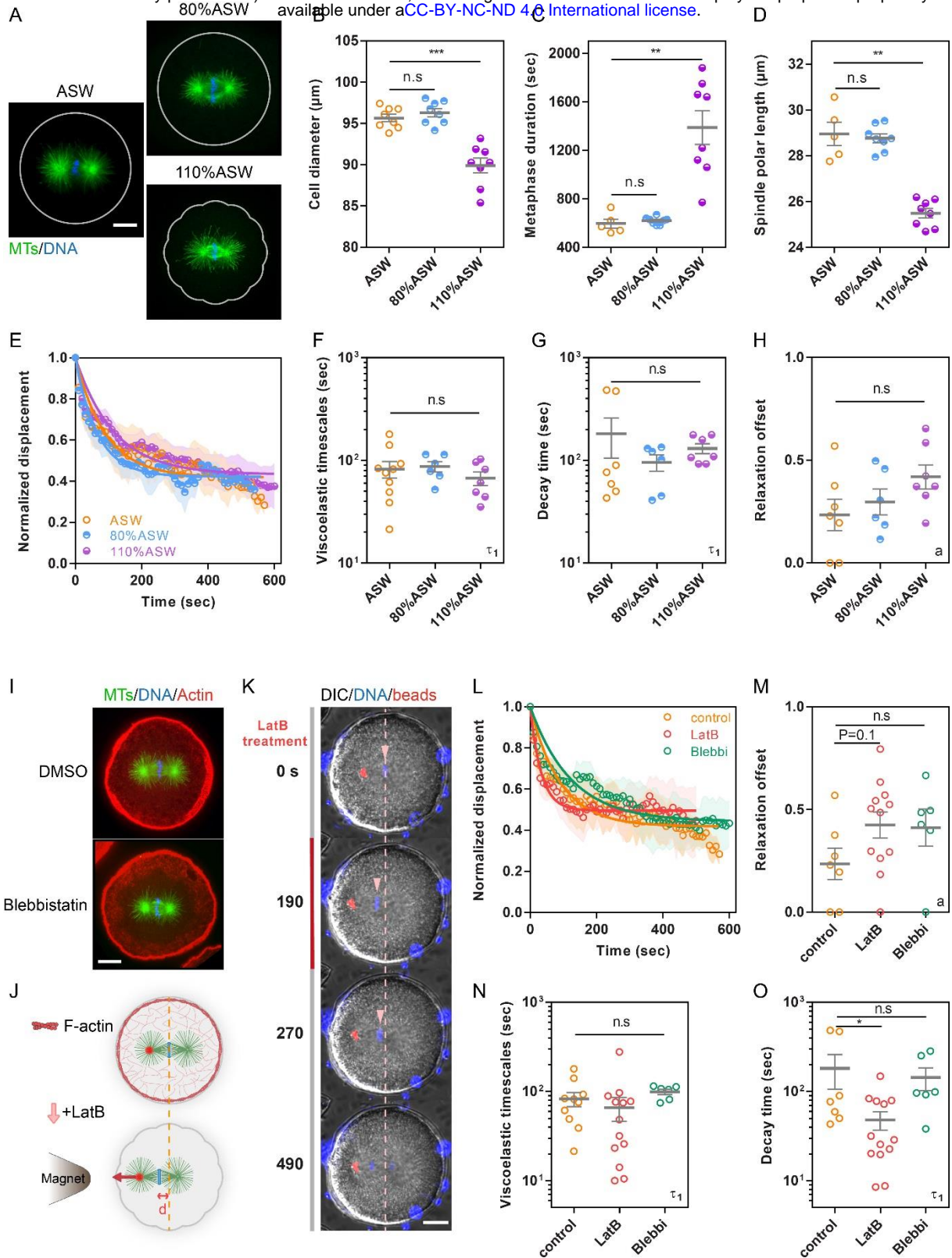
Figure S4. Impact of cytoplasm density, F-actin and myosin II on viscoelastic forces on spindles from bulk cytoplasm. (A) Confocal images of eggs treated 5min with normal ASW (Artificial Sea Water), 80% ASW or 110%ASW, fixed and stained for MTs and DNA. **(B-D)** Diameter, metaphase duration and spindle length of eggs in ASW (n=8) or 5 min after treatment in 80% ASW (n=8) and 110% ASW (n=8). **(E)** Time evolution of the normalized displacement back to the cell center in controls (n=10) and in cells treated with 80% ASW (n=6) and 110% ASW (n=7). **(F-G)** Viscoelastic timescale, τ_1 measured during the rising pulling phase or the relaxation phase, in controls and cells treated with 80% ASW and 110% ASW. **(H)** Relaxation offset for controls and cells treated with 80% ASW and 110% ASW. **(I)** Confocal images of eggs treated with DMSO or Blebbistatin, fixed and stained for MTs, DNA and F-actin. **(J)** Scheme representing F-actin structures and *in vivo* force application on metaphase spindles in the presence of Latrunculin B. **(K)** Time-lapse of eggs treated with Latrunculin B to depolymerize F-actin and assayed for spindle displacement under force and relaxation. **(L)** Time evolution of the normalized displacement back to the cell center in controls (n=10), in cells treated with Latrunculin B (n=13) and in cells treated with Blebbistatin (n=6). **(M)** Relaxation offset for controls and cells treated with Latrunculin B and Blebbistatin. **(N-O)** Viscoelastic timescale, τ_1 measured during the pulling phase or the relaxation phase, in controls and cells treated with Latrunculin B and Blebbistatin. Error bars and shades correspond to +/- S.E.M and +/- S.D/2 respectively. Results were compared by using a two-tailed Mann–Whitney test. n.s, $P > 0.05$, *, $P < 0.05$, **, $P < 0.01$, ***, $P < 0.001$. Scale bars, 20 μm.

A + MG132

Kymograph of spindle relaxation

Time (sec): 0 – 300

beads (red), DNA (blue)

T=120s

B T=490s

C T=1240s

D T=1960s

E translation / rotation — Displacement/force (μm/pN) vs Time (sec); Arc, d

F Restoring stiffness (pN/μm) — n.s — translation, rotation — κ

G Drag (pN.sec/μm) — P=0.1 — translation, rotation — γ_1

H Decay time (sec) — P=0.09 — translation, rotation — τ_1

Figure S5. Role of the duration of force application in the dissipation of elastic energy, and differences between translational and rotational behavior. (A-D) Kymographs following beads and DNA overtime for the relaxation phases upon force applications of varying durations. The dotted arrowhead marks the initial position of spindle centers at the onset of the relaxation phase, and the filled arrowhead indicates the final position after 300s**. (E)** Comparison of translational and rotational creep behavior using the arc length tracking the spindle pole displacement as a measurement of effective displacement during rotational motion. **(F-H)** Restoring stiffness, drags and decay times measured for translation vs rotation. Open and closed dots correspond respectively to data obtained in control or MG132 treated cells. Error bars and shades correspond to +/- S.E.M and +/- S.D/2 respectively. Results were compared by using a two-tailed Wilcoxon test. n.s, $P > 0.05$. Scale bars, 20 μm.
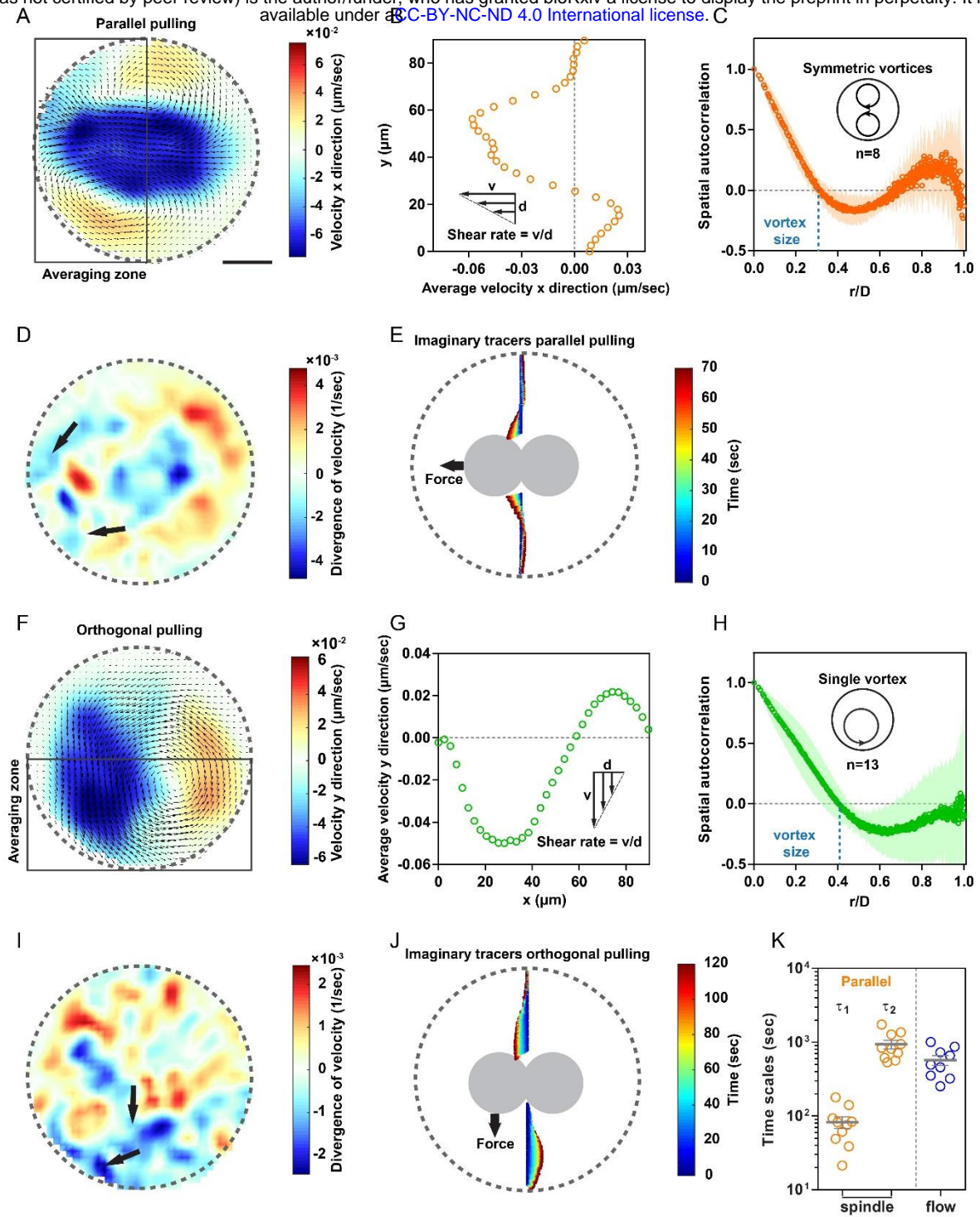
Figure S6. Flows of cytoplasm elements and associated analysis during spindle translational and rotational motions. (A) Flow maps of a representative spindle pulled with magnetic forces parallel to its axis, superimposed with a color map of the flow velocity projected along the x-axis. **(B)** Averaged velocity component in the horizontal direction (x) in the box indicated in A, plotted as a function of the vertical distance (y), used to compute shear rates. **(C)** Spatial autocorrelation averaged on 8 individual experiments and flow analysis used to compute flow vortex sizes. **(D)** Color maps of the divergence of the velocity used to locally map zones where the cytoplasm matrix may compress (indicated with arrows). **(E)** Trajectories of imaginary flow tracers placed along the direction orthogonal to the spindles used to visualize net displacement of cytoplasm material as a function to the distance to the spindle. **(F-J)** Similar analysis as in (A-E) for spindles pulled orthogonal to the spindle axis. **(K)** Viscoelastic timescales τ_1 and τ_2 extracted for spindles from rising curves and compared to a time-scale calculated from the inverse of the shear rate from the flow maps. Error bars and shades correspond to +/- S.E.M and +/- S.D respectively. Scale bars, 20 μm.

Supporting movie legends

Movie S1. **Metaphase spindles remain still in the cell center.** Time-lapse of a zygote with DNA labelled with Hoechst, through metaphase, followed by a time-lapse of an egg treated with MG132 to prolong metaphase. Time is in min:sec.

Movie S2. **Metaphase spindle pulled parallel to their long axis with magnetic tweezers in live cells.** Time-lapse of 2 metaphase spindles pulled with magnetic forces along their long axis and let to recoil and divide. Beads are labelled in red and DNA in blue. Time is in min:sec.

Movie S3. **Metaphase spindle pulled orthogonal to their long axis with magnetic tweezers in live cells.** Time-lapse of 2 metaphase spindles pulled with magnetic forces orthogonal to their long axis, let to recoil and divide. Beads are labelled in red and DNA in blue. Time is in min:sec.

Movie S4. Magnetized oil droplets pulled in the cytoplasm and let to recoil. Time-lapse of an egg injected with an oil droplet containing magnetic beads, pulled with magnetic tweezers and let to recoil. Time is in min:sec.

Movie S5. Serial Block Face images of metaphase cytoplasmic components with corresponding 3D pixel classification. Z-stacks of the metaphase cytoplasm with classified chromosomes (blue), ER (purple), Yolk (yellow) and Mitochondria (red). Close up views of the spindle region are presented at bottom.

Movie S6. Cytoplasm flows during parallel and orthogonal pulls. Time-lapse of an egg in which the metaphase spindle was pulled parallel to its long-axis, superimposed by the flow vector maps in red; followed by a similar time-lapse for an orthogonal pull. Time is in min:sec.